Available online at www.keaipublishing.com/en/journals/journal-of-magnesium-and-alloys/

ScienceDirect

Journal of Magnesium and Alloys xxx (xxxx) xxx

www.elsevier.com/locate/jma

Full Length Article

Achieving strength-ductility-biodegradation synergy in a low-alloyed Mg-Sn-Li-Ca alloy via multi-polarization of texture and second phases

Dongsheng Han[a,b,1], Zilin Li[c,1], Zhangzhi Shi[c,*], Laszlo S Toth[d,e], Werner Skrotzki[f], Benoit Beausir[d], Zhonghua Du[a], Sen Yang[g], Fengjian Shi[h], Amélie Fillon[i], Helene Birembaux[j], Mohammed El Ganaoui[k], Cai Chen[b,*], Luning Wang[c]

[a] *School of Mechanical Engineering, Nanjing University of Science and Technology, Nanjing 210094, PR China*
[b] *Sino-French Engineer School, Nanjing University of Science and Technology, Nanjing 210094, PR China*
[c] *State Key Laboratory for Advanced Metals and Materials, School of Materials Science and Engineering, University of Science and Technology Beijing, Beijing 100083, PR China*
[d] *Université de Lorraine, CNRS, Arts et Métiers ParisTech, LEM3, Metz F-57000, France*
[e] *Institute of Physical Metallurgy, Metal forming and Nanotechnology, University of Miskolc, Miskolc 3515, Hungary*
[f] *Institute of Solid State and Materials Physics, Dresden University of Technology, Dresden 01062, Germany*
[g] *School of Materials Science and Engineering, Nanjing University of Science and Technology, Nanjing 210094, PR China*
[h] *School of Materials Science and Engineering, Jiangsu University of Science and Technology, Zhenjiang 212003, PR China*
[i] *Université de Rennes, INSA Rennes, CNRS, ISCR-UMR 6226, Rennes F-35000, France*
[j] *Arts et Métiers Institute of Technology, LaBoMaP, Cluny F-71250, France*
[k] *Laboratoire d'Etudes et de Recherche sur le Matériau Bois (LERMAB), Université de Lorraine, Longwy F-54400, France*

Received 30 October 2025; received in revised form 29 December 2025; accepted 16 January 2026
Available online xxx

Abstract

Wrought Mg-Sn alloys are promising for biomedical applications due to their excellent biocompatibility, biodegradability, low density, and high specific strength. However, the poor corrosion resistance and mechanical performance of conventional wrought Mg-Sn alloys limit their clinical applications in load-bearing components. To address these challenges, an extrusion-shearing (ES) process was applied to a novel low-alloyed Mg-Sn-Li-Ca alloy, tailoring its microstructure and texture for comparison with conventional extrusion (EX). The ES process resulted in a significantly refined and homogeneous microstructure, reducing the average grain size to 4.9 μm, less than half of the EX sample (11.1 μm). Instead of a typical single-pole texture component with <10−0>//extrusion direction (ED) in EX sample, the ES sample showed a multipolar texture consisting of three fiber texture components: C1 (115°, 90°, 0∼60°), C2 (175°, 90°, 0∼60°), and P (150°, 0∼90°, 30°). The ES sample achieved a tensile yield strength of 231.8 MPa and elongation of 14.3%, representing improvements of 10.4% and 24.3% over the EX sample, respectively. Microstructural evolution combined with visco-plastic self-consistent modeling revealed that the C1 component promotes {10–12} twinning in the ES samples. The enhanced strength and ductility of the ES samples stemmed from multi-polarization of texture, second-phase distribution, and more homogeneous grain refinement. Moreover, corrosion behavior in α-minimum essential medium was investigated through immersion and electrochemical tests. Although both EX and ES samples exhibited similar high biocompatibility, the biodegradation rate of the ES samples was only 68.2% of the EX sample under immersion. In the ES sample, the multidirectional second-phase streamlines (i.e., multi-polarization of the second phase) inhibited pitting corrosion; the more corrosion-resistant {1–217} planes are nearer to the sample surface in grains with C1 texture component, replacing the {10–10} planes in the EX samples. These findings provide a viable strategy for advanced biodegradable implants via crystallographic engineering.

Keywords: Mg-Sn-Li-Ca alloy; Extrusion-shearing; Multi-polarization texture; Strength-ductility-biodegradation.

Peer review under the responsibility of Chongqing University.
* Corresponding authors.
E-mail addresses: ryansterne@163.com (Z. Shi), cai.chen@njust.edu.cn (C. Chen).
[1] These authors contributed to the work equally and should be regarded as co-first authors.

https://doi.org/10.1016/j.jma.2026.102000

Please cite this article as: D. Han, Z. Li, Z. Shi et al., Achieving strength-ductility-biodegradation synergy in a low-alloyed Mg-Sn-Li-Ca alloy via multi-polarization of texture and second phases, Journal of Magnesium and Alloys, https://doi.org/10.1016/j.jma.2026.102000

1. Introduction

Magnesium and its alloys have attracted considerable attention for biomedical applications owing to their low density, appropriate mechanical properties, excellent biodegradability, and favorable biocompatibility [1–4]. Their use as implant materials can eliminate the need for secondary revision surgeries [5–7]. However, the large-scale applications remain limited by several key factors [4,8,9,10], such as low strength, poor ductility, and insufficient corrosion resistance. Alloying is an important method to improve the mechanical properties and corrosion resistance of Mg alloys. For example, the addition of rare earth (RE) elements such as Gd, Y, or Nd [11–13] can promote grain refinement, introduce abundant second-phase particles, and promote the formation of rare earth textures (RE-texture) [14]. This improves strength, ductility, and corrosion resistance. However, high-performance RE-Mg alloys rely on a relatively high addition of RE elements, which leads to a high production cost [15,16] and raises biocompatibility concerns [7]. To overcome these drawbacks, scholars have developed a series of low-alloyed RE-free Mg alloys [9,17,18], including Mg-Ca [19], Mg-Zn [20], and Mg-Sn [21,22] based alloys. Among them, Mg-Sn alloys present more significant aging strengthening response, better biocompatibility, and biodegradability, making them promising candidates for biomedical materials [23–25]. For load-bearing implants, such as bone implant devices and vascular stents [25–27], adequate strength and ductility are required to endure physiological stress, while maintaining structural integrity for at least 12 weeks [5,28] for the body's self-repair [25]. Nevertheless, the conventional wrought Mg-Sn alloys display limited corrosion resistance [24,29,30], leading to an excessively rapid biodegradation rate. Achieving an optimal balance among strength, ductility, and biodegradation rate remains a key challenge for the practical application of Mg–Sn alloys in biomedical implants.

Strengthening and toughening of Mg-Sn alloy are primarily achieved through grain refinement [31,32]. Extrusion (EX) is an efficient and cost-effective processing technique for producing fine-grained Mg alloys [15], and it has also become one of the main strengthening methods for fabricating high-performance Mg-Sn alloys [22,33–35]. For instance, after being processed by EX (at an extrusion ratio of 23), the average grain size of low-alloyed Mg-2Sn-1Li-1Al alloy [36] could be refined to 1.37 μm, and the tensile strength of the alloy reached 291 MPa with an elongation of 9%. By optimizing the heat treatment process before extrusion, Zhou et al. [22] obtained a high-performance Mg-6Sn-3Zn-0.3Zr alloy with a tensile strength of 325 MPa and balanced elongation of 27.6%. Although Mg-Sn alloys with excellent mechanical properties can be prepared through extrusion, some shortcomings still exist. Non-uniform grain refinement is commonly observed in extruded Mg-Sn alloys [22,33], characterized by elongated coarse grains along the extrusion direction (ED) [22,37]. Such microstructural heterogeneity enhances the mechanical anisotropy of the alloy [38], which is undesirable for biomedical applications requiring resistance to multi-directional physiological loading.

In addition, due to the limited activation of the slip system at room temperature, the extrusion of Mg-Sn alloys is usually carried out at high temperatures (~300 °C) [22,25,35]. However, the solid solubility of Sn atoms in the Mg matrix is highly temperature-dependent. At 561 °C, approximately 14.5 wt.% Sn can be incorporated into the Mg matrix [39], but only ~0.45 wt.% at 200 °C [40]. Consequently, abundant coarse Mg_2Sn particles (>1 μm) [33,35] form and align along the ED in hot extruded Mg-Sn alloys. These particles act as micro-galvanic couples with the Mg matrix, accelerating the corrosion rate [41]. Gong et al. [28] reported that the corrosion rate of extruded Mg-2Sn-1Zn-1Y-0.3Zr alloy could be 1.7 times higher than that of its as-cast counterpart. The main reason for this phenomenon is that the coarse Mg_2Sn particles provide more active sites for galvanic corrosion. Another characteristic of extruded Mg-Sn alloys is the development of a strong basal texture [33]. For wrought Mg alloys, the corrosion behavior also depends on the crystallographic orientations [42]. According to Song [43], the {0001} basal plane of Mg is considered to be more corrosion resistant than the {10–10} prismatic plane. Thus, the strong basal texture not only leads to mechanical anisotropy [44] but also to an anisotropic corrosion behavior [45].

In recent years, the coordinated optimization of microstructure and texture has become a key strategy for developing high-performance wrought Mg alloys [46–50]. The main objective is to control the grain size and weaken the basal texture [47,51]. Introducing severe plastic shear strain during deformation is particularly effective [52–54], as it promotes uniform grain refinement, redistribution of precipitates, and texture weakening. Therefore, equal channel angular pressing (ECAP) has been applied to fabricate the high-performance biodegradable Mg alloys, including Mg-RE [55], Mg-Zn [56] and Mg-Sn [57,58] based alloys. Generally, multi-pass ECAP deformation improves both corrosion resistance and mechanical properties of Mg alloys compared to as-cast or homogenized alloys with coarse-grains [56,59,60]. However, such improvements are often limited or one-sided, constrained by excessive grain size and unbefitting texture modification. For instance, while grain refinement can enhance strength, an excessively small grain size may accelerate corrosion. As reported [61], the electrochemical corrosion rate of the Mg alloys can increase by up to 60% when the grain size of Mg alloys is refined from 3 μm to 1.4 μm. Studies [57,58,62] show that ECAP often induces pronounced grain refinement (<2 μm) in Mg-Sn alloys due to severe plastic shear strain deformation, which in turn increases corrosion susceptibility. As reported by Zemková et al. [55] and Martynenko et al. [63], although multi–pass ECAP further enhances the mechanical performance of extruded Mg alloys through grain refinement and the introduction of shear texture components, it simultaneously leads to a decline in corrosion resistance. This effect results not only from grain size but also from texture evolution. Since the ECAP deformation can introduce some grains with prismatic and pyramidal planes paralleled to

Please cite this article as: D. Han, Z. Li, Z. Shi et al., Achieving strength-ductility-biodegradation synergy in a low-alloyed Mg-Sn-Li-Ca alloy via multi-polarization of texture and second phases, Journal of Magnesium and Alloys, https://doi.org/10.1016/j.jma.2026.102000

the corrosion surface, the corrosion resistance should decrease due to their higher surface energy [56]. Moreover, recent studies [44,64] also reported that the texture modification induced by ECAP may also lead to a decrease in yield strength due to the texture softening effect. Therefore, precisely identifying the texture that simultaneously benefits both mechanical properties and biodegradation performance is critical. Additionally, ECAP-processed Mg samples typically have limited dimensions, and the need for continuous processing increases technical complexity. Achieving a synergistic improvement in strength, ductility, and controlled biodegradation of Mg-Sn alloys through coordinated microstructure and texture design still requires innovative approaches.

In this study, extrusion (EX) and extrusion-shearing (ES) processes were employed to fabricate a low-alloyed Mg-3.0Sn-0.5Li-0.2Ca alloy (wt.%; denoted as TLX alloy). With the ES processing, an alloy with a uniformly refined microstructure and multipolar texture was successfully obtained, resulting in significantly improved mechanical properties and biodegradation resistance compared with conventional EX samples. This study systematically characterized the microstructure, deformation texture, mechanical behaviors, biocompatibility, and biodegradation rate of the deformed alloy. The influence of shear strain introduced during ES on the microstructure, second phase distribution, and texture evolution of TLX alloy was systematically examined. Visco-plastic self-consistent (VPSC) modeling was used to simulate the contribution of individual texture components to strength and ductility. Finally, the underlying mechanisms governing the synergistic optimization of strength, ductility, and biodegradation through uniform microstructure refinement and texture multi-polarization were elucidated.

2. Materials and methods

2.1. Materials and deformation techniques

Alloy ingots with a nominal composition of Mg-3.0Sn-0.5Li-0.2Ca alloy (wt.%, referred to as TLX alloy) were prepared from high-purity raw materials (99.9 wt.% pure Mg, Sn, Li, and Ca) by using vacuum induction melting under argon atmosphere. Following casting, homogenization treatment of the ingots was conducted at 500 °C for 5 h. Then, the homogenized ingots were preheated at 350 °C for 30 min prior to deformation. Subsequently, two deformation routes were applied: extrusion (EX) and extrusion-shearing (ES) [65] processes. As shown in Fig. 1, in a single deformation pass of ES process, an extrusion (extrusion ratio of 4) with two-pass ECAP deformation (channel angle of 105°) can be achieved. During the continuous ECAP deformation zone, the two shear directions are opposite. For subsequent tests on microstructure, mechanical properties, and corrosion behavior, the sample collection locations are also presented in Fig. 1. Both EX and ES were performed at 350 °C with an extrusion speed of 20 mm/s. The extrusion ratio of the EX process is 16, corresponding to a von-Mises equivalent strain of ~2.8. For the ES process, as mentioned in our previous studies [44,65], the calculated von-Mises equivalent strain is ~2.5.

2.2. Characterization of microstructure, texture and mechanical properties

The microstructure of the processed samples was observed through optical microscopy (OM), scanning electron microscopy (SEM, FEI Quanta 250F) equipped with an energy-dispersive spectrometer (EDS), and transmission electron microscopy (TEM, FEI Tencai 20). For OM and SEM analyses, both the longitudinal (ED-ND) and cross-sectional (ND-TD) planes of the extruded bar were mechanically polished to a mirror finish. Picric acid and a 4% solution of nitric alcohol were used as etchants to reveal grain morphology and second-phase particles. For TEM observations, the samples (3 m disc) were prepared by an ion milling instrument (GATAN 691) at 6 kV. To identify the type of precipitation, X-ray diffraction (XRD) was performed with a scan rate of 2°/min.

Texture evolution and dynamic recrystallization behavior were examined via electron backscatter diffraction (EBSD, ZEISS Gemini SEM 460) on the longitudinal (ED-ND) plane. Texture and slip/twin activities during deformation were simulated using visco-plastic self-consistent (VPSC) modeling [11], considering basal ⟨a⟩, prismatic ⟨a⟩, pyramidal ⟨$c + a$⟩ slips, and {10–12} extension twinning. The simulation results were validated by post-fracture EBSD analysis of the tensile samples. Mechanical properties were evaluated through quasi-static tensile tests conducted on a SHIMADZU machine at a strain rate of 1.5×10^{-3} s^{-1}. The mechanical properties of each sample were tested five times, with the standard deviations calculated as error.

2.3. Electrochemical measurements and immersion tests

In order to evaluate the electrochemical corrosion rate of the TLX samples, electrochemical measurements were conducted, using a three-electrode cell system (ModuLab XM, Ametek, U.S.) in α-minimum essential medium (α-MEM) at 37 ± 1 °C. The TLX alloy specimens with an exposed area of 0.2827 cm^2 were taken as working electrodes, with a Pt foil as counter electrode and a saturated calomel electrode (SCE) as reference electrode. Prior to each measurement, the alloy surfaces were stabilized through 600-s open circuit potential (OCP) testing. Tests were performed using electrochemical impedance spectroscopy (EIS) with a sinusoidal amplitude of 10 mV over the frequency range of 10^5 to 10^{-2} Hz. Potentiodynamic polarization (PDP) tests were executed from −0.2 V vs. OCP to −1.1 V vs. SCE at a scan rate of 1 mV/s. EIS data were fitted using the ZSimpWin software with an equivalent circuit. For Mg alloys, the electrochemical corrosion rate (P_i, mm/year) can be calculated using the corrosion current density (i_{corr}, mA/cm^2) by the following equation [66]:

$$P_i = 22.85 \cdot i_{corr} \quad (1)$$

Early biodegradation behavior of the EX and ES samples was investigated via in vitro immersion tests, where samples

Please cite this article as: D. Han, Z. Li, Z. Shi et al., Achieving strength-ductility-biodegradation synergy in a low-alloyed Mg-Sn-Li-Ca alloy via multi-polarization of texture and second phases, Journal of Magnesium and Alloys, https://doi.org/10.1016/j.jma.2026.102000

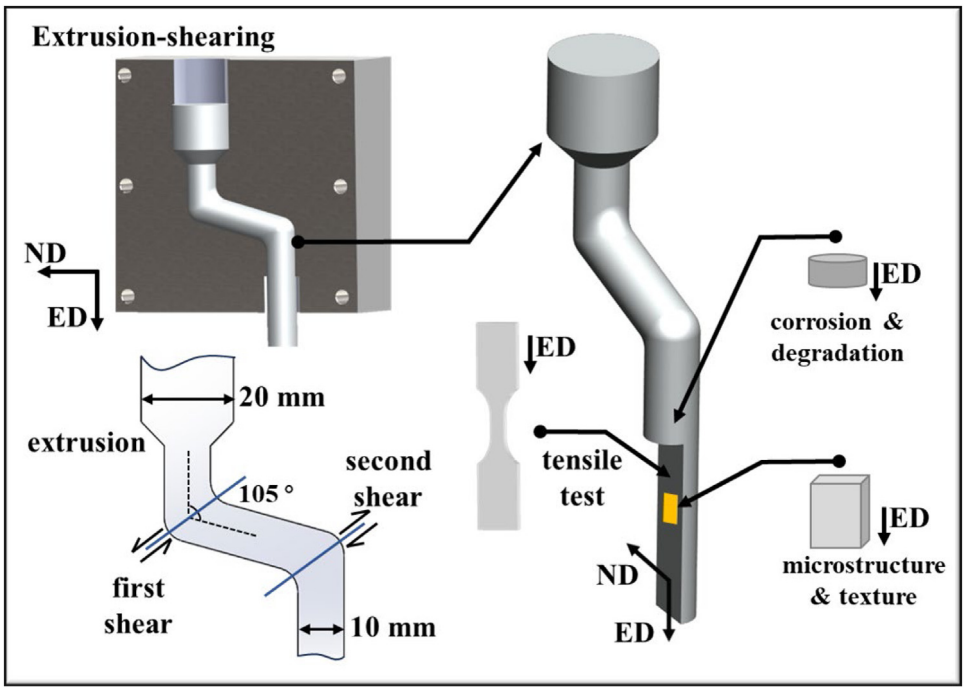

Fig. 1. Schematic of extrusion shearing process.

were immersed in α-MEM at 37 ± 0.5 °C for 24 h with a ratio of 1.25 cm^2/mL (sample area to solution volume). The samples were cut into disks with a diameter of 10 mm and a thickness of 2 mm. After immersion, the samples were submerged in a chromate solution (200 g/L CrO_3 + 10 g/L $AgNO_3$) for 10 min to remove corrosion products. Finally, the samples were washed in anhydrous alcohol by ultrasonic cleaning and dried before weighing. The average biodegradation rates (*BR*, mm/year) can be calculated in terms of the weight loss method according to the following equation [67]:

$$BR = \frac{8.76 \times 10^4 \times \Delta W}{A \times t \times \rho} \quad (2)$$

where ΔW is the weight loss in units of g, A (in cm^2) is the exposed surface area, t (in h) is the total immersion time, and ρ (in g/cm^3) is the density of the alloy. All procedures were replicated three times to verify repeatability, and the standard deviation was used as the margin of error. Ion concentrations were measured by inductively coupled plasma atomic emission spectrometry (ICP-AES). Surface morphologies of the immersed samples were observed using a white light interferometer microscope (WLIM, Contour GTK, Bruker).

2.4. Cytotoxicity tests

Referring to ISO 10993-12 [68], indirect cytotoxicity tests were performed using mouse osteoblast cells (MC3T3-E1) to evaluate the in vitro cytotoxicity of the TLX samples. Before the tests, the sterilized TLX samples were soaked in α-MEM at 37 °C for 24 h to prepare the sample extracts. The ratio of sample surface area to α-MEM volume was 1.25 cm^2/mL. MC3T3-E1 cells were seeded at a density of 2×10^4 cells/mL and cultured for 24 h. Cells subsequently were incubated with the sample extracts at varying concentrations (25%~100%) for 24 h and 72 h. Complete culture medium was served as the negative control, while medium containing 10% dimethyl sulfoxide (DMSO) was regarded as the positive control.

Cell viability (*CV*) was quantified using the Cell Counting Kit-8 (CCK-8) assay, calculated as:

$$CV = \left[\left(OD_e - OD_p\right)/\left(OD_n - OD_p\right)\right] \times 100\% \quad (3)$$

where OD_e, OD_p, and OD_n represent the optical density (*OD*) of the experimental group (cultured in the extracts), the positive and the negative control group, respectively. The cells cultured with the sample extracts for 24 h were stained with a mixture of calcein-acetoxymethyl (calcein-AM) and propidium iodide (PI). The cell morphologies were observed by an inverted fluorescence microscope (Axio Vert.A1, ZEISS).

2.5. Alkaline phosphatase (ALP) tests

After 4 days and 7 days of culture in 100% extract, MC3T3-E1 cells were stained using the BCIP/NBT alkaline phosphatase color development kit (Beyotime, Shanghai, China) and observed under a microscope (Zeiss Axiovert 200 M, Germany). For quantitative ALP activity analysis, the ALP testing kit (Jiancheng Bio-engineering Research Institute of Nanjing, China) was employed, and the *OD* values were measured at a wavelength of 520 nm using a multimode plate reader (EnSpire, PerkinElmer, USA).

Please cite this article as: D. Han, Z. Li, Z. Shi et al., Achieving strength-ductility-biodegradation synergy in a low-alloyed Mg-Sn-Li-Ca alloy via multi-polarization of texture and second phases, Journal of Magnesium and Alloys, https://doi.org/10.1016/j.jma.2026.102000

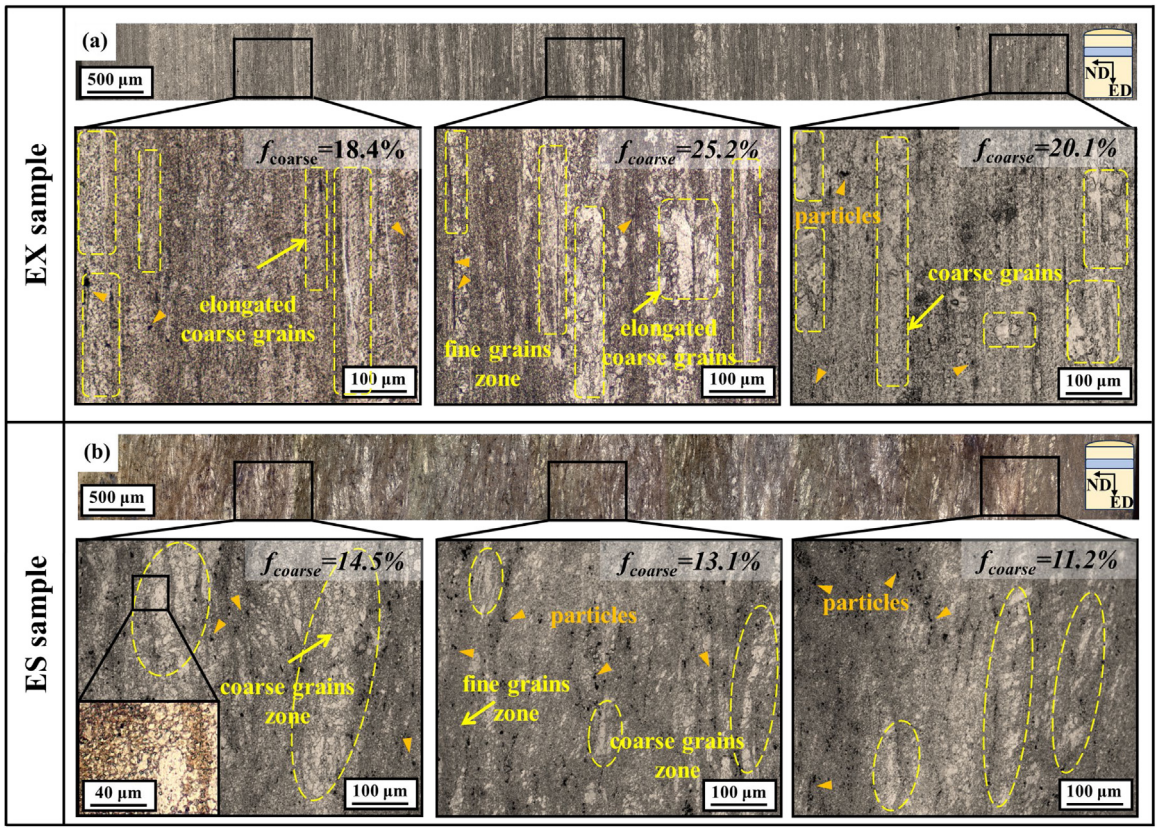

Fig. 2. Microstructure of the processed samples observed by OM on ED-ND plane: (a) EX sample; (b) ES sample.

3. Results

3.1. Microstructures

The OM images of the processed EX and ES samples are shown in Fig. 1, which displays the microstructure on the ED-ND plane. It can be observed that the microstructure morphology and deformation uniformity are significantly affected by the EX and ES processes. As shown in Fig. 2a, the EX sample primarily consists of elongated fibrous grains and fine equiaxed grains. The elongated grains tend to be parallel to ED, with lengths even exceeding 500 μm. Statistical analysis reveals that the area fractions of elongated grains at the left/right edges of the EX sample are 18.4% and 20.1%, respectively. In the center of the EX sample, the fraction of those grains increased to 25.2%, which indicates that the deformation is nonuniform between the edge and the center of the EX sample. The microstructure of the ES sample is shown in Fig. 2b. Under the combined extrusion and shear strain path (ECAP) during the ES process, more uniform grain refinement was achieved. From the locally magnified microstructure at the left edge of the ES sample in Fig. 2b, it can be seen that the diameter of fine grains in this sample is <5 μm. Although coarse grains still appear in the ES sample, their size is notably smaller (~50 μm) than that of the elongated grains in the EX sample. Moreover, these coarse grains in the ES sample no longer exhibit a fibrous morphology and are not parallel to ED. It is worth mentioning that the area fraction of coarse grains was also significantly reduced in the ES sample. The results reveal that the ES process benefits a more uniform refinement of the microstructure. Additionally, numerous particles appear in both EX and ES samples; further comparative particle analyses were performed using SEM and TEM.

Fig. 3a and b present the EBSD inverse pole figure (IPF) maps of EX and ES samples (accounting for >3000 grains each). The corresponding grain size distribution and dynamic recrystallization (DRX) maps of EX and ES samples were calculated by using ATEX software [69], shown in Fig. 3c-e. The grains with internal disorientation angles <2° were classified as recrystallized (DRXed) grains. After being processed by the conventional EX process, the average grain size (surface-weighed) of the EX sample is 11.1 μm with 75.3% DRXed grains. Unexpectedly, some abnormally coarse grains in the EX sample were also classified as recrystallized grains due to the low internal disorientation. For the ES sample, the average grain size is 4.9 μm, significantly smaller than that of the EX sample. However, the area fraction of recrystallized grains is about 10% smaller under ES. Fig. 3c shows that the area fraction of the grains with grain size smaller than 10 μm is higher in the ES sample, and it exhibits a more uniform grain size distribution without undesired large grains (>20 μm). The disorientation distributions of EX and ES samples are illustrated in Fig. 3f. In both

Please cite this article as: D. Han, Z. Li, Z. Shi et al., Achieving strength-ductility-biodegradation synergy in a low-alloyed Mg-Sn-Li-Ca alloy via multi-polarization of texture and second phases, Journal of Magnesium and Alloys, https://doi.org/10.1016/j.jma.2026.102000

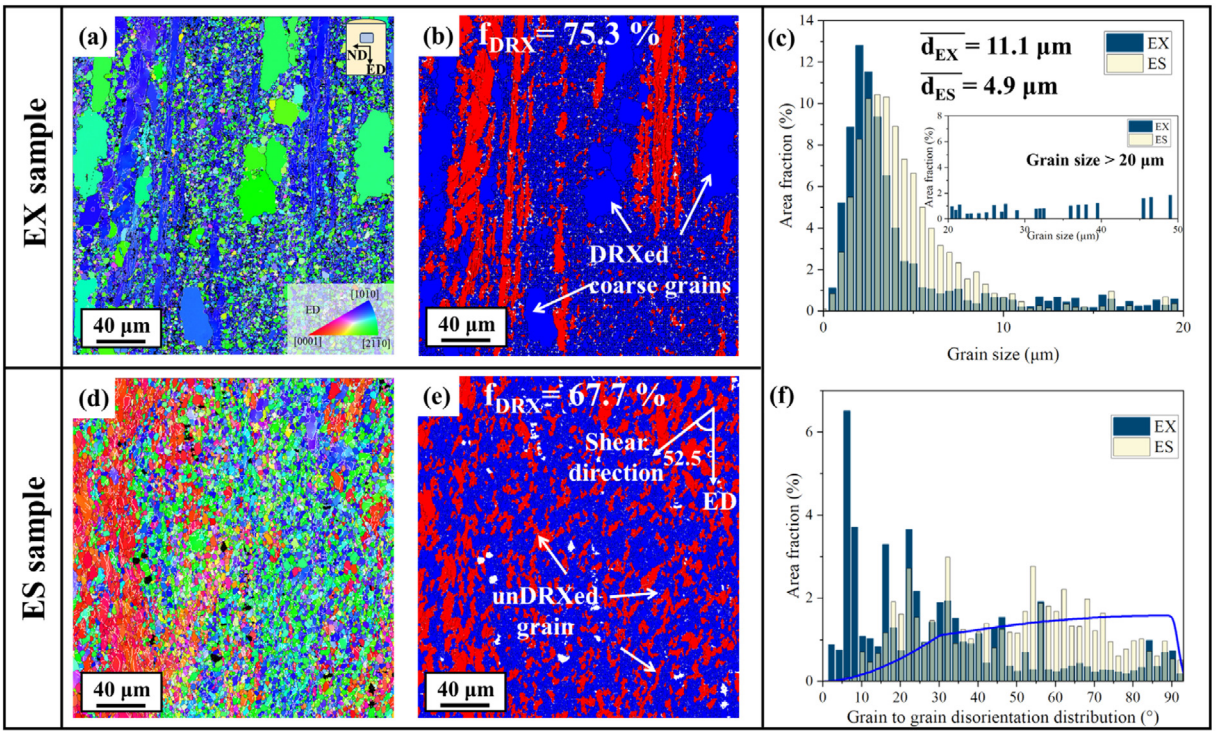

Fig. 3. EBSD analysis: IPF maps of (a) EX sample and (b) ES sample; (c) grain size distribution; (d-e) dynamic recrystallization analysis (the DRXed grains are marked by red and the unDRXed grains in blue); (f) disorientation distribution (Mackenzie distribution in blue line for random disorientation distribution).

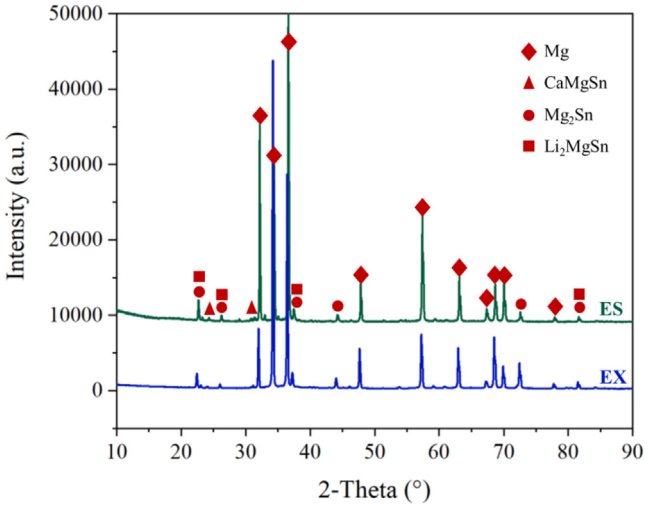

Fig. 4. XRD patterns of the EX and ES samples.

EX and ES samples, their disorientation distributions do not conform to the Mackenzie distribution [70], which represents random disorientation of Mg alloy.

Fig. 4 displays the XRD patterns of EX and ES samples. Previous studies [36,71,72] report that the addition of Sn and Li will promote the formation of Mg_2Sn and Li_2MgSn second phases in Mg alloys. Due to their similar lattice constants [72] (0.6759 and 0.6764, respectively), their diffraction peaks should overlap in XRD patterns. In the TLX alloy, 3.0 wt.% Sn, 0.5 wt.% Li, and 0.2 wt.% Ca were added. The XRD results confirm that Mg_2Sn, Li_2MgSn, and CaMgSn precipitates are the possible main precipitates in both EX and ES samples.

In Fig. 5, the micron-scale particles in the EX and ES samples were characterized by SEM. Fig. 5a and b illustrates the distribution of particles on different cross-sections of the EX and ES samples. In the EX sample, particles are continuously distributed along different mutually parallel straight lines that are also parallel to ED. As shown in Fig. 5b, the shear deformation in the ES sample results in a multidirectional particle distribution, where the particles are mainly distributed along discontinuous streamlines. In addition, the particle clustering is more pronounced in the EX sample with more densely spaced particle lines, while the ES sample shows a more dispersed particle distribution. In contrast to the uniform linear alignment in the EX sample, the particles in the ES sample exhibit a discontinuous, curvilinear distribution along multiple orientations, with each trajectory inclined at a distinct angle to the ED. This multi-oriented and morphologically varied distribution of second phase particles is defined as a multi-polarized distribution. Particles with three distinct morphologies were found in both the EX and ES samples: coarse particles with elliptical shape (A), short rod-shaped particles (B), and small cubic particles (C). The quantity of B-type and C-type particles is much greater than that of A-type particles. The EDS results of those particles reveal (Table 1) that A-type particles could be Sn-rich or CaMgSn particles, while both B-type and C-type particles are typical Mg_2Sn precipitates. Fig. 5d presents the particle size distribution of the EX and samples on the ED-ND plane, obtained by Image-Pro Plus software. To ensure statistical accuracy, three images per sam-

Please cite this article as: D. Han, Z. Li, Z. Shi et al., Achieving strength-ductility-biodegradation synergy in a low-alloyed Mg-Sn-Li-Ca alloy via multi-polarization of texture and second phases, Journal of Magnesium and Alloys, https://doi.org/10.1016/j.jma.2026.102000

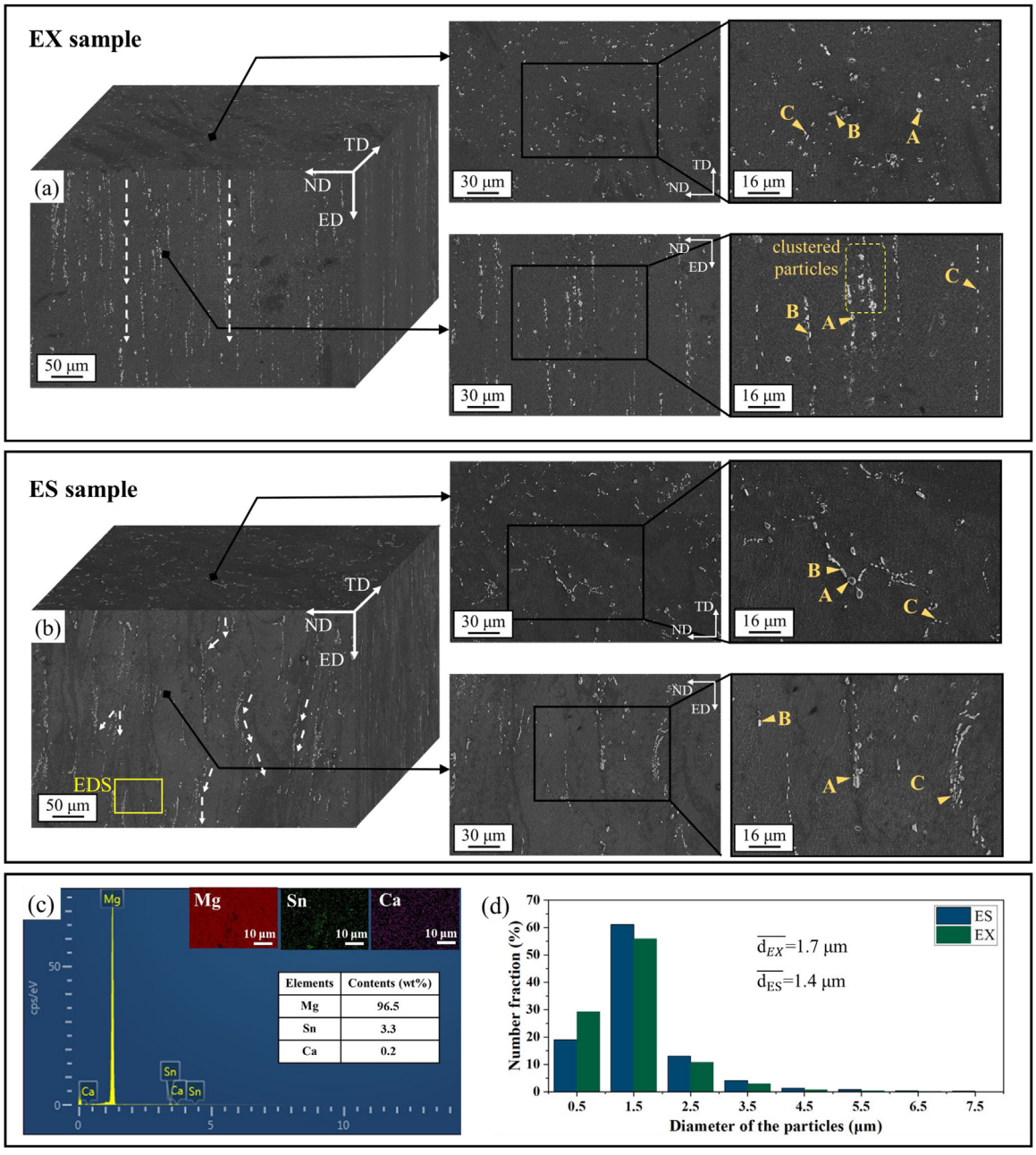

Fig. 5. SEM morphologies of (a) EX sample and (b) ES sample, (c) EDS mapping and energy spectrum, (d) particle size distribution.

Table 1
Components analysis of the marked particles in Fig. 4 by EDS point scanning. The phase analysis was based on the XRD pattern in Fig. 3.

Sample	Plane	Point	Mg (at%)	Sn (at%)	Ca (at%)	Possible phase
EX	ND-TD	A	25.4	74.6	/	Sn-rich particles
		B	64.0	36.0	/	Mg_2Sn
		C	70.5	29.5	/	Mg_2Sn
	ED-ND	A	36.6	34.6	28.8	CaMgSn
		B	70.2	29.8	/	Mg_2Sn
		C	67.2	32.8	/	Mg_2Sn
ES	ND-TD	A	28.3	38.7	33.0	CaMgSn
		B	67.7	32.3	/	Mg_2Sn
		C	61.5	38.5	/	Mg_2Sn
	ED-ND	A	50.9	42.3	6.8	Sn-rich particles
		B	71.4	28.6	/	Mg_2Sn
		C	69.1	30.9	/	Mg_2Sn

Please cite this article as: D. Han, Z. Li, Z. Shi et al., Achieving strength-ductility-biodegradation synergy in a low-alloyed Mg-Sn-Li-Ca alloy via multi-polarization of texture and second phases, Journal of Magnesium and Alloys, https://doi.org/10.1016/j.jma.2026.102000

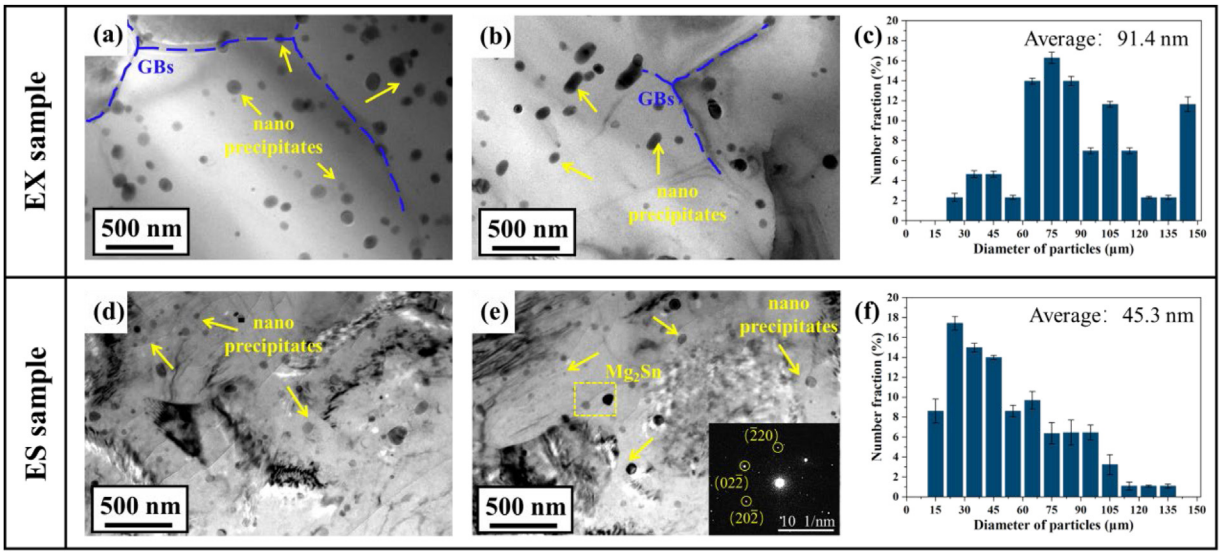

Fig. 6. TEM bright field images of the (a-b) EX sample and (d-e) ES sample with pattern taken from the yellow dotted box. (c, f) The size distribution of nano precipitates.

ple were analyzed, and particles smaller than 0.5 μm were excluded. The average diameters of the particles are 1.7 μm and 1.4 μm in the EX and ES samples, respectively. The results show that 84.8% of particles in the ES sample are smaller than 1.5 μm, while it is 80.2% in the EX sample. SEM and XRD results confirm that the predominant second-phase particles in the deformed alloy are Mg_2Sn.

Besides micron-scale particles, nano precipitates are also commonly formed in Mg-Sn alloys. As shown in Fig. 6, numerous nano precipitates are observed in TEM bright-field images in both EX and ES samples. In the EX sample, spherical nano precipitates are mainly distributed within the grains, with a few located at grain boundaries. The distribution of nano precipitates is relatively dispersed in both EX and ES samples. Nevertheless, the average diameter of the nano precipitates in the ES sample is ~45.3 nm, much smaller than that of ~91.4 nm in the EX example. According to the diffraction pattern in Fig. 6e, the nano precipitates are Mg_2Sn.

3.2. Crystallographic texture

The textures of the deformed samples are presented in Fig. 7, by both pole figures (PFs) and inverse pole figures (IPFs). During EX deformation, the sample develops a typical extruded fiber texture of hexagonal metals (texture intensity index: 4.1), with predominantly [10–10] oriented parallel to ED. A minority (~17.5%) of grains have [2–1–10]//ED.

For the ES sample, a multipolar texture with three distinct {0002} orientations is observed in the {0002} PF with maxima near ED, ND, and TD (center of the PF). It has been reported by Benoit et al. [74] that various ideal shear texture components (B, C1-C2, Y1-Y2, and P) could be introduced in Mg alloy by applying ECAP deformation. In this study, two continuous ECAP processes (route C) with a die angle of 105° were achieved following the extrusion. The ideal shear texture components introduced by route C ECAP with this die angle are shown in Fig. 6c. Compared with the ideal shear texture components with the experimental results, it confirms that the main texture components in the ES sample are C1, C2, and P shear components. The texture intensity of the ES sample is 2.4, which is weaker than the EX sample. As shown in Fig. 7d and f, the 3D maps illustrated the textures of the EX and ES samples based on the orientation distribution function (ODF), which were reconstructed using MATLAB. The EX sample shows a continuous extrusion fiber texture, where the Euler angles of the three main components in the ES sample were calculated to be C1 (115°, 90°, 0~60°), C2 (175°, 90°, 0~60°), and P (150°, 0~90°, 30°). The c-axis of grains related to C1, C2, and P components are 10°~40° clockwise rotated from ED, −15°~25° anticlockwise rotated from ND, and parallel to TD, respectively. The volume fractions of C1, C2, and P components are 34.2%, 48.6%, and 16.3%, respectively. In the ES sample, there are also some grains that have the c-axis parallel to ED (volume fraction of 0.9%), which constitute the "C-texture" component [75]. As reported in our previous study [44], in ES processed Mg alloys, the c-axis of grains is oriented within several distinct angular ranges relative to the ED. This orientation characteristic leads to the appearance of multiple texture components in pole figures and/or inverse pole figures, which are widely spaced with relatively high intensity. Such a texture feature is defined as texture multi-polarization. The textures in Fig. 6 demonstrate that texture weakening and multi-polarization could be achieved readily in ES-processed Mg alloy by introducing simple shear strain.

3.3. Mechanical properties

Fig. 8a presents the tensile engineering stress-strain curves of the EX and ES samples measured via the digital image correlation (DIC) technique. The corresponding yield strength (YS), ultimate tensile strength (UTS), and elongation to fail-

Please cite this article as: D. Han, Z. Li, Z. Shi et al., Achieving strength-ductility-biodegradation synergy in a low-alloyed Mg-Sn-Li-Ca alloy via multi-polarization of texture and second phases, Journal of Magnesium and Alloys, https://doi.org/10.1016/j.jma.2026.102000

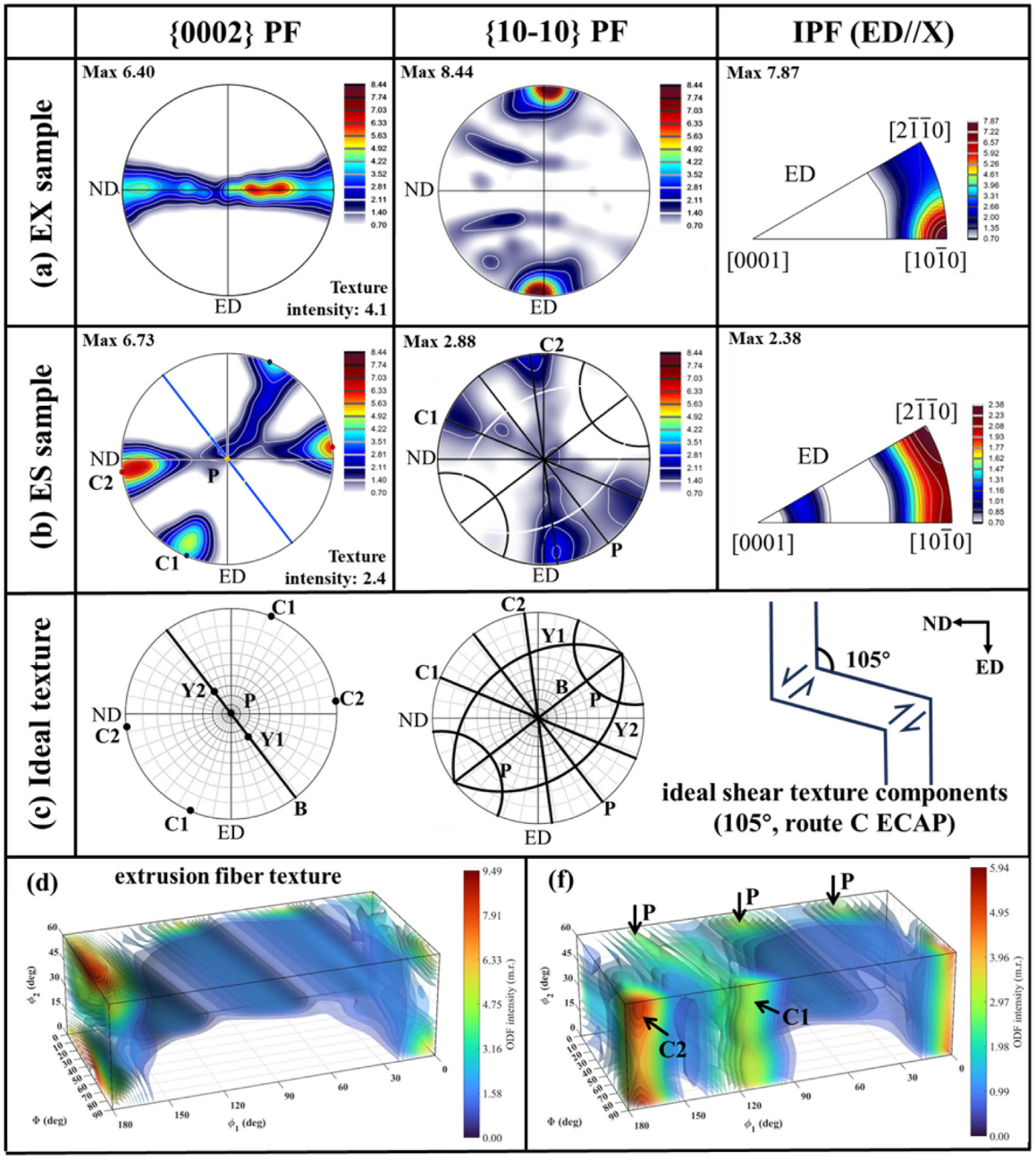

Fig. 7. Orientation distributions within the (a) EX and (b) ES samples in {0002}, {10-10} PFs and IPFs of the ED axis and (c) ideal shear texture components of ECAP processed Mg (die angle of 105°, 2 passes in route C) [73]. 3D ODF map of (d) EX sample and (f) ES sample.

ure (EL) are summarized in Table 2. The EX sample has a YS and UTS of 209.9 MPa and 261.6 MPa, respectively, with an elongation of only 11.5% The ES sample shows better mechanical properties, with YS, UTS, and EL increasing to 231.8 MPa, 304.2 MPa, and 14.3%, respectively.

Fig. 8b summarizes the mechanical properties of previously reported extruded Mg-Sn alloys [21,24,30,35–37,76–82] with comparable compositions to the present work, including Mg-Sn binary alloys as well as ternary and quaternary Mg-Sn based alloys with total alloy content below 9 wt.% Among them, the extruded alloys with an alloy content larger than 4 wt.% are marked with orange graphics, as shown in Fig. 8b. In Table 2, the mechanical properties of the low-alloyed Mg-Sn alloys (alloying addition <4 wt.%) are evaluated together with their deformation conditions. These results demonstrate that the ES process affords a markedly strength-ductility balance in Mg-Sn-based alloys compared to conventional extrusion at equivalent strain levels and alloying contents.

After tensile testing, the fracture morphologies and microstructures of the EX and ES samples were characterized using secondary electron (SE) and backscattered electron (BSE) images, as shown in Fig. 9. As can be seen that the EX sample exhibits brittle fracture characteristics with multiple cleavage planes observed in Fig. 9a. In contrast, the

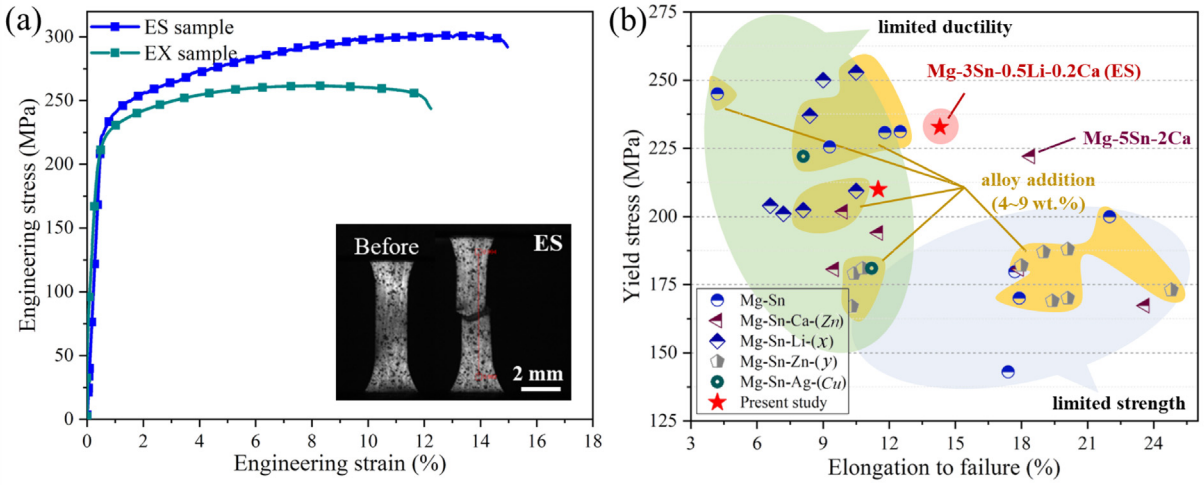

Fig. 8. (a) Mechanical properties of the EX and ES samples; (b) comparison of the yield stress and elongation of extruded Mg-Sn based alloys with Refs [21,24,30,35–37,76–82].

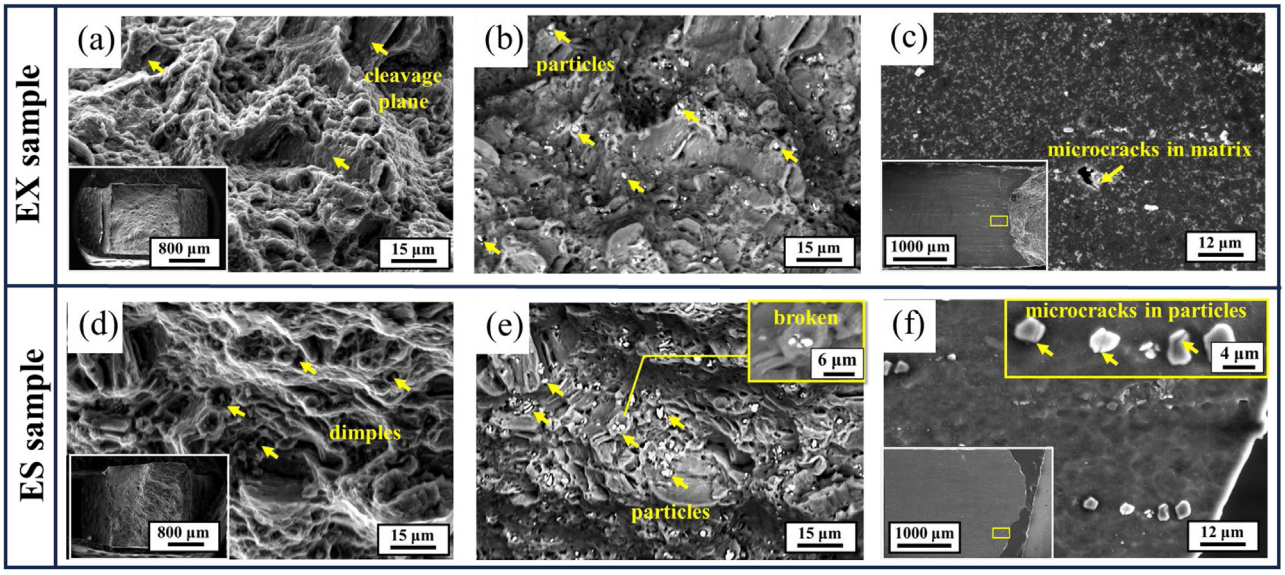

Fig. 9. Fracture morphology and microstructure of the (a-c) EX and (d-f) ES samples after the tensile test: (a, c, d, f) SE; (b, e) BSE.

Table 2
Mechanical properties of the EX, ES samples and extruded low-alloyed (<4 wt.%) Mg-Sn based alloys from Refs [30,36,76,78].

Compositions (wt%)	Extrusion temperature (°C), speed (mm/s)	Von-Mises equivalent strain	YS (MPa)	UTS (MPa)	EL (%)
Mg-3Sn-0.5Ca-0.2Li (ES)	300, 22.0	2.5	231.8 ± 3.5	304.2 ± 4.8	14.3 ± 0.5
Mg-3Sn-0.5Ca-0.2Li (EX)	300, 22.0	2.8	209.9 ± 6.3	261.6 ± 5.3	11.5 ± 6.3
Mg-3.6Sn [76]	300, 16.7	3.2	143.0	267.0	17.4
Mg-2Sn-1Li [76]	250, 0.35	3.1	204.0	242.0	6.6
Mg-2Sn-1.8Li [36]	250, 0.35	3.1	201.0	243.0	7.2
Mg-2Sn-1Al-1Li [36]	250, 0.35	3.1	250.0	291.0	9.0
Mg-2Sn-0.5Ca [30]	380, unreported	3.2	180.6	247.2	9.5
Mg-3Sn-0.5Ca [30]	380, unreported	3.2	193.5	253.2	11.5
Mg-1Sn-1Ca-0.5 Zn [78]	360, unreported	3.5	167.3	310.9	23.6
Mg-1Sn-2Ca-0.5 Zn [78]	360, unreported	3.5	180.7	300.0	17.9

Please cite this article as: D. Han, Z. Li, Z. Shi et al., Achieving strength-ductility-biodegradation synergy in a low-alloyed Mg-Sn-Li-Ca alloy via multi-polarization of texture and second phases, Journal of Magnesium and Alloys, https://doi.org/10.1016/j.jma.2026.102000

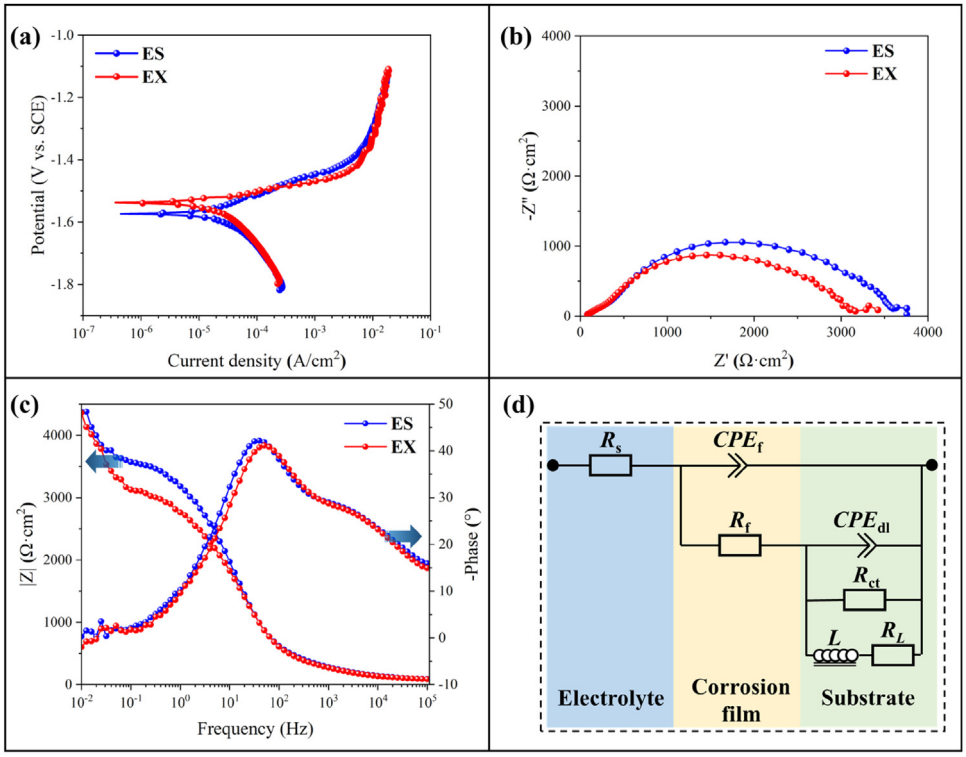

Fig. 10. Electrochemical analyses of the ES and EX alloys: (a) Polarization curves; (b) Nyquist plots; (c) Bode phase and modulus plots; (d) Corresponding equivalent circuit model.

Table 3
Electrochemical parameters derived from polarization measurements.

Samples	E_{corr} (V vs. SCE)	i_{corr} (μA/cm^2)	P_i (mm/y)
ES	−1.61 ± 0.01	4.27 ± 0.24	0.10 ± 0.01
EX	−1.54 ± 0.01	5.61 ± 0.33	0.13 ± 0.01

fracture morphology of the ES sample displays ductile fracture features, as evidenced by the abundant dimples visible in Fig. 9d, with numerous precipitates located in these dimples (Fig. 9e). Notably, particle fragmentation is observed in the dimples of the ES sample (Fig. 9d) which is absent in the EX sample. Fig. 9c and f show the microstructure on the lateral surfaces of the two samples after the tensile test. The results indicate that the clustered precipitates in the EX sample triggered microcrack nucleation in the matrix, thereby impairing the ductility of the alloy. In the ES sample, the dispersion of micron particles does not promote crack formation. Instead, the particles tend to fracture from within.

3.4. Electrochemical corrosion behavior

Fig. 10a shows the PDP curves of the EX and ES samples tested in α-MEM. The corresponding electrochemical parameters are summarized in Table 3. The ES sample exhibits a lower corrosion current density (i_{corr} = 4.270 μA/cm^2) compared to the EX sample (i_{corr} = 5.641 μA/cm^2). The calculated corrosion rates (P_i values in Table 3) also indicate that the ES sample exhibits enhanced corrosion resistance. Nyquist plots (Fig. 10b) of the ES and EX samples both feature a high-frequency capacitive loop and a minor low-frequency inductive loop. The larger diameter of the capacitive loop of the ES sample indicates superior corrosion resistance. This finding is also supplemented by Bode plots (Fig. 10c), where the ES sample exhibits slightly higher phase angle maxima and impedance modulus (|Z|), reaffirming its better corrosion resistance.

The Nyquist plots are fitted with an equivalent circuit (Fig. 10d), and the related fitted parameters are listed in Table 4. The equivalent circuit incorporates Constant Phase Elements (*CPE*) to describe the non-ideal capacitive behavior, which consists of the following elements: solution resistance (R_s), components related to the corrosion product layer (R_f and CPE_f), charge transfer resistance (R_{ct}), double-layer capacitance (CPE_{dl}), electrochemical inductance (L), and inductive resistance (R_L) [83]. L corresponds to an inductive behavior associated with localized film breakdown or intermediate adsorption phenomena. The higher R_f and R_{ct} values of the ES sample indicate better corrosion resistance than the EX sample [84]. Low χ^2 values demonstrate an excellent reliability of the fitting results.

4. Discussion

4.1. Dynamic recrystallization and texture evolution

Compared to the EX sample, the ES sample exhibits a significantly weaker texture with multipolar components (texture

Table 4
The EIS results fitted by the equivalent circuit.

	R_s ($\Omega\cdot cm^2$)	CPE_f		R_f ($\Omega\cdot cm^2$)	CPE_{dl}		R_{ct} ($\Omega\cdot cm^2$)	R_L ($\Omega\cdot cm^2$)	L ($H\cdot cm^{-2}$)	χ^2
		$Y_{0\text{-}f}$ ($s^n\cdot\Omega^{-1}\cdot cm^{-2}$)	n_f		$Y_{0\text{-}dl}$ ($s^n\cdot\Omega^{-1}\cdot cm^{-2}$)	n_{dl}				
ES	6.69×10	2.45×10^{-5}	0.55	5.44×10^{2}	7.36×10^{-6}	0.80	4.51×10^{3}	1.10×10^{4}	2.60×10^{2}	5.05×10^{-4}
EX	6.64×10	2.64×10^{-5}	0.55	5.19×10^{2}	6.95×10^{-6}	0.80	4.08×10^{3}	0.82×10^{4}	1.01×10^{2}	4.79×10^{-4}

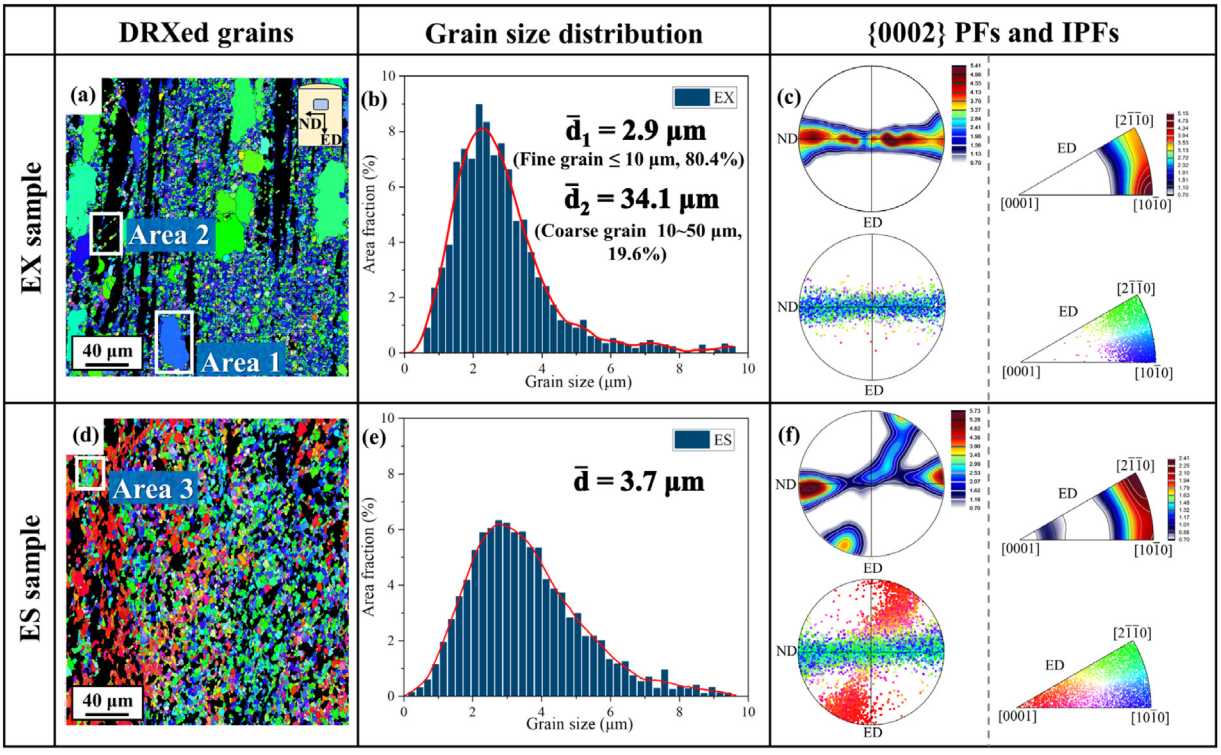

Fig. 11. (a, d) DRXed grains in IPF maps of the EX and ES sample, the analyses of the selected areas 1–3 are presented in Fig. 12; (b, e) grain size distributions; (c, f) {0002} PFs and IPFs and related single c-orientations presented by color-dots.

multi-polarization). Generally, the texture development during hot deformation is strongly related to DRX in Mg alloys. Therefore, a comparative analysis of the differences in DRX behaviors between EX and ES samples could help to reveal the mechanism for the texture multi-polarization in the ES sample. Fig. 11a and d show the IPF maps of DRXed grains of the EX and ES samples. The related grain size distributions and textures are shown in Fig. 11b and c and Fig. 11e and f.

The DRXed grains in the EX sample consist of fine grains with an average grain size of 2.9 μm and several abnormally large grains (average grain size of 34.1 μm, area fraction of 19.6%). The grain boundaries of the large grains are surrounded by numerous fine grains. Additionally, as can be seen within Area 2 of Fig. 11a, a fine-grained band of connected individual grains formed. This phenomenon is consistent with the characteristics of DRX induced by microshear bands [85]. During the hot deformation, microshear bands could provide nucleation sites for ultra-fine new grains, which significantly promotes the grain refinement. The corresponding crystallographic textures of DRXed grains in the EX sample are represented by {0002} PFs, IPFs, and their individual orientations (single c-orientations), as shown in Fig. 11c. The texture of the recrystallized and abnormally grown grains of the EX sample is comprised of two fibers along ED: [10-10] and weak [2-1-10].

In contrast to the bimodal grain size distribution in the EX sample, the DRXed grains of the ES sample display an unimodal distribution with an average grain size of 3.7 μm, which is comparable to that of the small grains in the EX sample. The texture of the DRXed grains in the ES sample is consistent with the multipolar textures of the entire sample shown in Fig. 7d, mainly composed of three shear texture components with regard to the ECAP shear system: C1, C2, and P. As shown by the single c-orientations in the PF and IPF of Fig. 11f, the C1 texture component corresponds to the red grains in the DRX map (Fig. 11d), while grains that form the C2 and P texture are in blue or green.

Three particular regions marked by white frames (Areas 1–3) in Fig. 11a and d are analyzed in more detail. Fig. 12

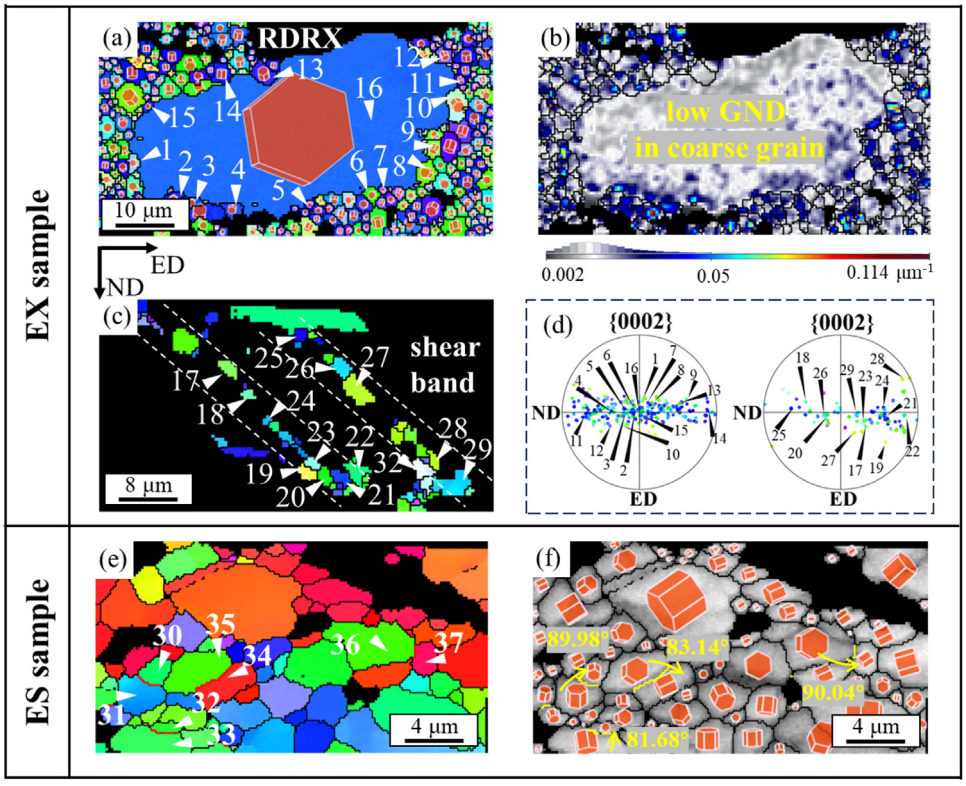

Fig. 12. Analysis of DRX mechanism (a-b) RDRX and related GND distribution; (c) microshear bands in EX samples; (d) {0002} pole figures with projections of the selected grains in (a) and (c); (e, f) twinning-related grains in ES sample.

shows the selected regions of the IPF maps with a high magnification. As shown in Fig. 12a, a representative coarse grain in the EX sample (Area 1) is redrawn with its adjacent fine grains. In addition, the corresponding oriented hexagonal unit cell of each grain is given in the map. By comparing the orientation of the abnormally coarse grain with that of the neighboring fine grains, it is evident that both grain fractions belong to the same double extrusion fibers. The geometrically necessary dislocation (GND) density of the abnormally grown grains is much smaller than that of the smaller DRXed grains (Fig. 12b). The result shows that dislocation motion is concentrated at the grain boundaries of the coarse grains and within the surrounding fine grains during the deformation. This phenomenon indicates a rotational dynamic recrystallization (RDRX) mechanism [54,86]. During the RRDX, a large number of dislocations are preferentially activated at the grain boundaries of coarse grains. Then, the RDRX will be completed with the sub-grain boundaries forming at the grain boundary of the large grain and rotating to high-angle grain boundaries. Once RDRX occurs, the large grain will be difficult to further refine because fewer dislocation motions could be activated within this coarse grain. Considering the mechanism of RDRX, it can also be recognized as a case of CDRX. The average grain size of the fine grains in Fig. 12a is about 2.9 μm. Although RDRX can introduce a significant number of fine grains to reduce the average grain size of the EX sample, it also exacerbates the nonuniformity of the microstructure.

Fig. 12c shows fine grains formed by microshear bands induced nucleation in the EX sample (Area 2), with an average grain size of about 1.7 μm. Microshear band-induced DRX is also a typical CDRX behavior [85]. Due to a higher degree of deformation in the shear band, the grains formed by this mechanism are usually smaller, allowing for significant grain refinement. In Fig. 12a and c, several DRXed fine grains are selected and their projections on the {0002} PFs are presented in Fig. 12d This demonstrates that the fine grains formed by RDRX mechanisms and microshear band-induced DRX in the matrix belong to the same texture fibers.

Fig. 12e displays the local microstructure selected from Fig. 11d of the ES sample (Area 3). The grain boundaries of grains in Fig. 12e were identified by the ATEX software; some grain boundaries were determined as {10–12} extension twin (ET) boundaries (marked in red line). It suggests that during the ES process, {10–12} ETs may have been activated to promote twinning-induced dynamic recrystallization (TDRX). To make a more accurate judgment of this inference, the Euler angles of grains on either side of the twin boundaries in Fig. 12e were calculated and listed in Table 5, with the corresponding disorientation angles. For the activation of {10–12} ETs, a ~86.3° rotation should be introduced between the Mg matrix and twinned areas. The disorientation angles between these grain pairs are approximately 81°~90°, consistent with the misorientation of {10–12} ETs. This further confirms that TDRX is a possible dynamic recrystallization mechanism in the ES sample. New grains nucleated during

Please cite this article as: D. Han, Z. Li, Z. Shi et al., Achieving strength-ductility-biodegradation synergy in a low-alloyed Mg-Sn-Li-Ca alloy via multi-polarization of texture and second phases, Journal of Magnesium and Alloys, https://doi.org/10.1016/j.jma.2026.102000

Table 5
Euler angles of grains marked in Fig. 10e and disorientation angles of neighboring grains.

Grains	$\phi 1$ (°)	φ (°)	$\phi 2$ (°)	Disorientation angles (°)
30	2.5	145.9	40.7	89.98
31	179.2	123.7	11.4	
32	8.5	108.5	40.9	81.68
33	144.9	166.9	0.3	
34	115.5	80.9	33.2	83.14
35	123.7	163.8	35.1	
36	86.1	167.6	56.7	90.04
37	124.0	80.2	18.6	

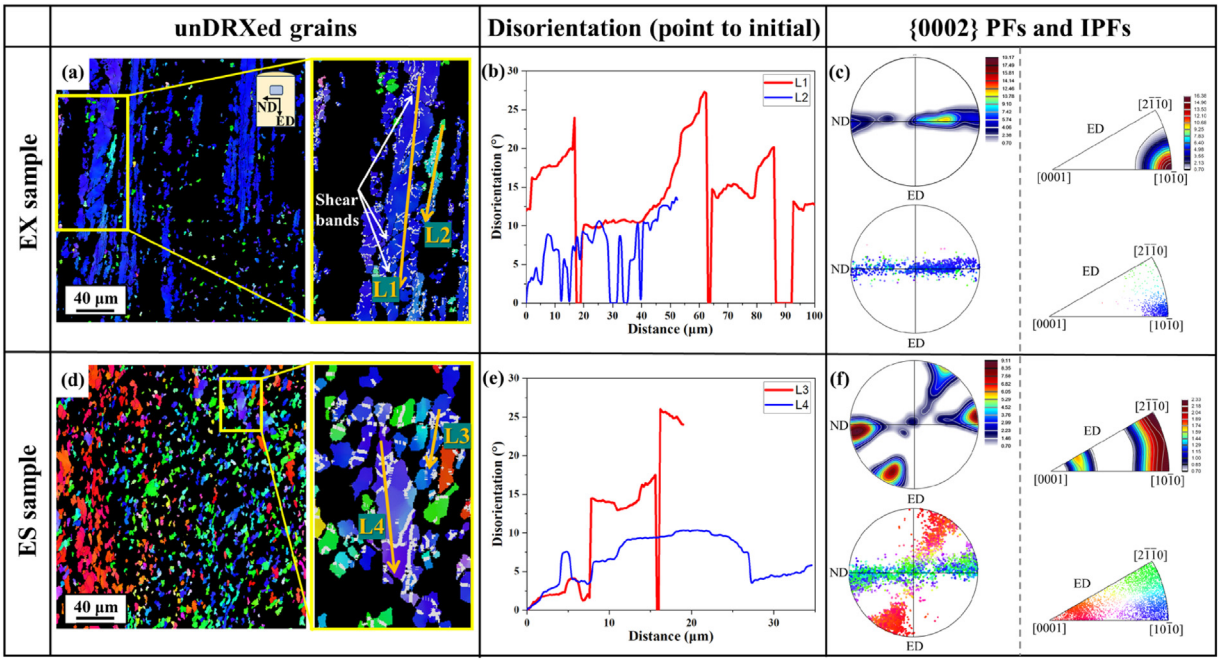

Fig. 13. (a, d) unDRXed grains of the EX and ES sample, the LAGBs in the local enlarged maps are labeled with white lines; (b, e) disorientation evolution from point to initial point (L1-L4); (c, f) {0002} PFs and IPFs.

TDRX exhibit significant orientation variations, which contribute to the weakening of the shear texture. In the ECAP process of Mg alloys, the development of C1 and C2 textures is predominantly controlled by the activation of pyramidal $<c + a>$ slip system [73]. Furthermore, twinning activation has been proven to facilitate the initiation of pyramidal $\langle c + a \rangle$ slip [87]. Microstructural evidence of retained {10–12} twin boundaries in the ES sample demonstrates that twinning activation plays a pivotal role in developing the multipolar textures.

By analyzing the sub-grain boundaries and disorientation distributions in unrecrystallized (unDRXed) grains in the EX and ES samples, the differences in continuous dynamic recrystallization (CDRX) behavior between the two samples can be revealed. As shown in Fig. 13a and c, the unDRXed grains in the EX sample have a relatively uniform orientation. The [10–10] axis of most of the elongated grains is parallel to ED. Only a small fraction of grains is oriented with [2-1-10]//ED. As shown in the enlarged local area of Fig. 13a, low-angle grain boundaries (LAGBs, <15°) are marked with white lines. It is obvious that abundant LAGBs exist within the elongated grains. These LAGBs extend from the grain edges into the interior, but do not traverse the entire grain. Additionally, considering the microstructure in Fig. 12a, the elongated grains are segmented into several new grains by microshear bands. The disorientation evolution along trace lines L1 and L2 is quantitatively analyzed for two unDRXed grains belonging to different fibers of the EX sample, as shown in Fig. 13c.The results show that the two unDRXed grains exhibit a continuous transformation of disorientation, which is evidence for CDRX. Notably, line L1 intersects several microshear bands, resulting in a sharp drop in disorientation at these crossing points. However, this microshear-induced grain segmentation shows negligible influence on the orientation of the deformed matrix grains. In contrast, unDRXed and DRXed grains in the ES sample belong to the same shear components (Fig. 13d

and f). The local high-magnification observations in Fig. 13d reveal that LAGBs in the unDRXed grains of the ES sample traverse almost across the entire grains. Quantitative analysis in Fig. 13e confirms that these well-developed LAGBs could induce substantial disorientation changes (up to 25°) within the matrix.

Based on the analysis presented in Section 4.1, the following conclusions can be drawn: (1) In the EX sample, CDRX is the primary mechanism for grain refinement. The DRXed fine grains generated through CDRX maintained a strong crystallographic relationship with the basal-oriented parent grains, leading to typical extrusion fibers. (2) During the ES process, the texture multi-polarization can be attributed to the strain path change from extension to shear. The imposed shear strain leads to the formation of three crystallographically distinct shear components of unDRXed grains and significantly promotes the activation of deformation twinning. Subsequently, grain refinement through CDRX and TDRX contributes to the formation of the multipolar textures and texture weakening.

4.2. Strength-ductility

After being processed by ES, the TLX alloy exhibits better mechanical properties than the EX sample. The YS and EL of the ES sample increased by 10.4% and 24.3% compared with the values of the EX sample. The mechanical properties of wrought Mg are mainly influenced by solid solution elements, grain size, precipitates, and crystallographic texture. In this study, there are no changes in the alloying elements.

4.2.1. Grain refinement and precipitation

Based on the Hall-Petch relationship [88], the contribution of grain refinement to the YS of Mg alloy can be calculated:

$$\sigma_1 = \sigma_0 + k_y d^{-1/2} \tag{4}$$

Here, σ_0 is the yield stress of a magnesium single crystal, k_y is the Hall-Petch slope, and d is the average grain size. Generally, σ_0 and k_y are influenced by grain size and texture [88]. Due to the complex relationship between texture and these parameters, the Hall-Petch calculation in this study does not consider texture effects and only accounts for grain size. The influence of texture on yield strength will be calculated using the VPSC modeling in Section 4.2.2.

For the EX sample, the average grain size of DRXed fine grains is approximately 2.9 μm, while the average size of coarse grains is 30.7 μm. Based on reports by Tianshui Zhou et al. [22], the calculation parameters for small and large grains in the EX sample are determined as σ_0 = 124 and 78 MPa, k_y = 205 MPa and 507 MPa, respectively. The calculated contributions of fine grains and coarse grains to the strength of the EX sample are 244.4 MPa and 169.5 MPa, respectively. The grain size distribution in the ES sample is more uniform, with an average grain size of 4.9 μm. Using the calculation parameters of fine grains in the EX sample, the contribution of grain refinement to the strength of the ES sample is about 216.6 MPa. The presence of numerous large grains in the EX sample is the main factor limiting its yield strength. In reality, the large grains in the EX sample are not equiaxed. Their contribution to yield strength may be even lower than the calculated value.

In the EX and ES samples, the nano Mg_2Sn precipitates could have a significant strengthening effect on the YS. Generally, dispersed nano precipitates primarily strengthen the material through the Orowan dislocation-precipitate bypass mechanism under tension. The contribution of nano precipitates can be calculated using Eq. (5) [22,89]:

$$\sigma_2 = \frac{MGb}{2\pi\lambda\sqrt{1-v}} ln\frac{d_p}{r_0} \tag{5}$$

where M is the Taylor factor (2.38), G represents the shear modulus of Mg (17.2 GPa), and b is the magnitude of the Burgers vector (0.32 nm). The Poisson ratio υ is about 0.3. λ is the effective planar interparticle spacing, and d_p is the average diameter of the particles. r_0 is the cut-off radius of the dislocation core (normally equal to b). Based on the distribution of nano-sized precipitates shown in Fig. 6, the average sizes of precipitate particles in the EX and ES samples are 91.5 nm and 45.3 nm, respectively, with an interparticle spacing of approximately 400 nm. The calculated contributions of nano precipitates to the YS of the EX and ES samples are 35.1 MPa and 30.8 MPa, respectively. The difference in precipitate strengthening between the two samples is negligible. Besides the nano precipitates, both EX and ES samples contain numerous micron-sized particles. As shown in Fig. 9c and f, the random distribution of microscale precipitates in the ES sample is beneficial for the strength by preventing abnormal localized stress concentration.

4.2.2. Effect of texture multi-polarization

The EBSD results of the fractured EX and ES samples after the tensile test are shown in Fig. 14. The microstructure, twin boundary distribution, and the corresponding crystallographic texture are presented. As shown in Fig. 14a and d, the microstructure morphologies of the EX and ES samples are maintained, however, with obvious twinning activation. With the high-magnification microstructure images in Fig. 14b and e, the twin boundaries are highlighted with blue lines and drawn in the corresponding band contrast (BC) maps. In the EX sample, only a few spindle-shaped twins appear in the elongated large grains, while the ES sample exhibits abundant twin lamellas. Some grains in the ES sample even contain multiple paralleled twins. After the tensile test, the length fraction of twin boundaries reaches 11.4% in the ES sample (Fig. 14e). Crystallographic analysis using ATEX software identifies these deformation twins as {10–12} ETs. In Mg alloys, the {10–12} ET is the most easily activated twinning system at room temperature due to the lower critical resolved shear stress [90]. The activation of abundant twins improves the ductility of the ES sample. For EX sample, the texture remains the extrusion double fiber texture with a much stronger [10–10] fiber intensity (Fig. 14c) after fractured. However, as shown in Fig. 14f, the crystallographic texture of the fractured ES sample (Fig. 14f) has changed significantly compared to

Please cite this article as: D. Han, Z. Li, Z. Shi et al., Achieving strength-ductility-biodegradation synergy in a low-alloyed Mg-Sn-Li-Ca alloy via multi-polarization of texture and second phases, Journal of Magnesium and Alloys, https://doi.org/10.1016/j.jma.2026.102000

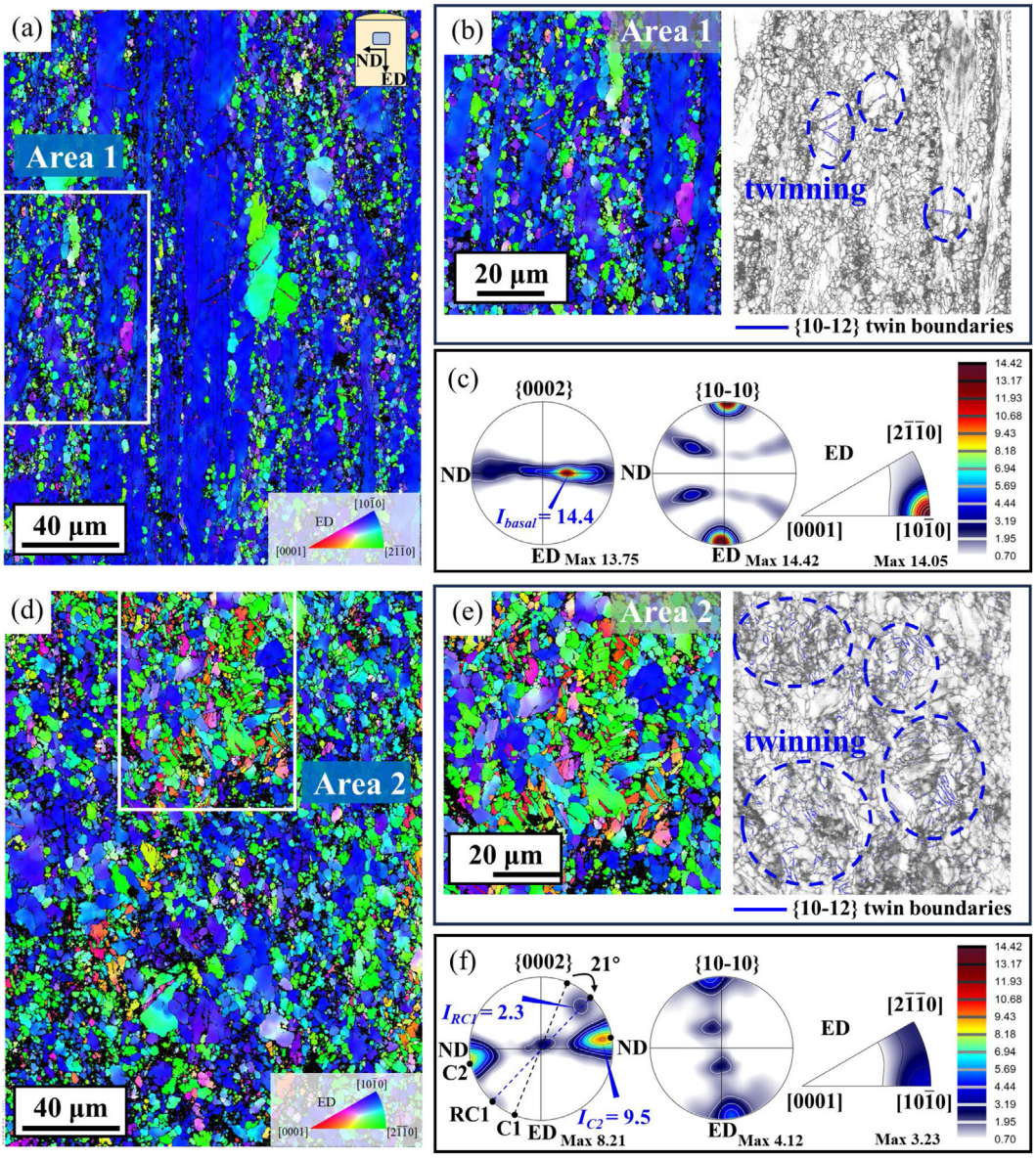

Fig. 14. EBSD results of fractured samples after tensile test: (a, d) IPF maps; (b, e) selected high-magnification maps with twin boundary distribution; (c, f) textures of fractured EX and ES samples.

the original texture in Fig. 7. Although the texture still exhibits three poles, the original C1 texture has disappeared. The newly formed texture component, labeled RC1, is clockwise rotated 21° from the original C1 texture tilted towards ND. As shown in the {0002} PF, the intensities of the RC1 and C2 textures are 2.3 and 9 m.r.d. In Fig. 14d, the area fractions of grains corresponding to the RC1, C2, and P texture components are 10.5%, 75.9%, and 13.6%, respectively. The texture evolution is towards the typical [10–10] tensile deformation fiber texture of hexagonal metals. The ESBD results preliminarily demonstrated that the improvement of texture multi-polarization on the ductility was achieved by promoting the activation of twinning.

In order to further reveal the effect of texture multi-polarization on the deformation mechanisms, VPSC modeling was established to fit the true stress-strain curve as well as simulate the consequent texture evolution of the ES sample during the tensile test. The VPSC simulation employs the Voce-hardening model [11], which can be expressed with the following function:

$$\tau(\Gamma)=\tau_0+(\tau_1+\theta_1\Gamma)\left(1-\exp\left(-\frac{\Gamma\theta_0}{\tau_1}\right)\right) \quad (6)$$

where τ_0 and θ_0 are the initial yield stress and hardening rate in the given slip system, and τ_1 and θ_1 determine the asymptotic hardening rate.

The Voce-hardening model considers the possible activation of basal slip, prismatic slip, pyramidal $<c+a>$ slip, and {10–12} twinning at room temperature. For each deformation mechanism, the four hardening parameters required for the

Please cite this article as: D. Han, Z. Li, Z. Shi et al., Achieving strength-ductility-biodegradation synergy in a low-alloyed Mg-Sn-Li-Ca alloy via multi-polarization of texture and second phases, Journal of Magnesium and Alloys, https://doi.org/10.1016/j.jma.2026.102000

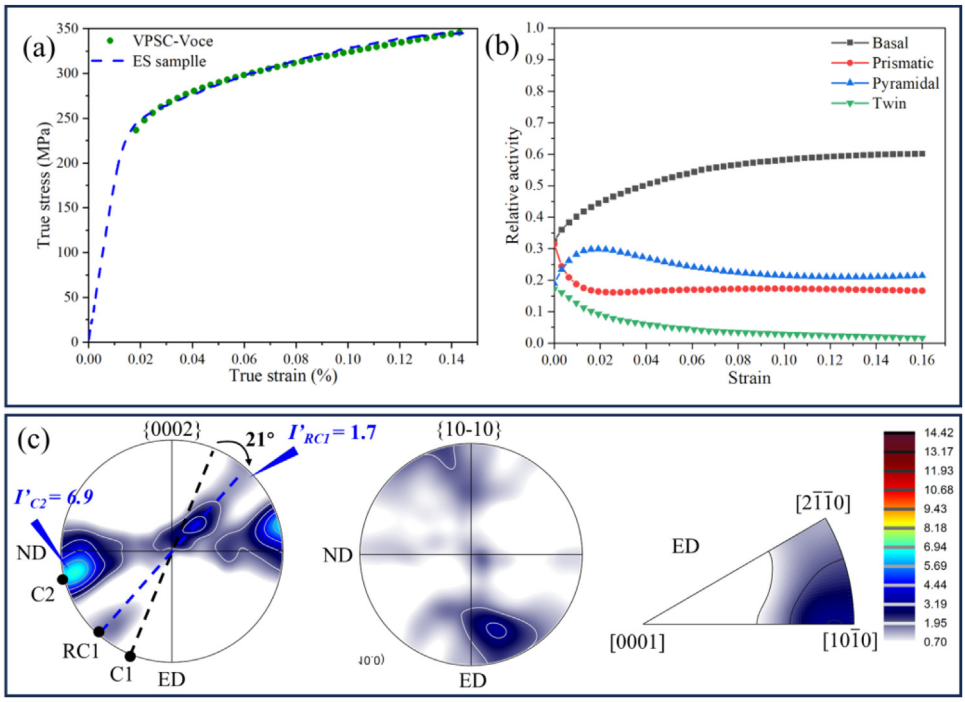

Fig. 15. VPSC simulation of the ES sample under tension: (a) Experimental and simulated true strain-true stress curves; (b) relative activation of basal, prismatic, pyramidal slip and {10–12} twinning; (c) simulated texture at fracture strain.

Table 6
Hardening parameters of VPSC modeling (unit is MPa).

Deformation mode	τ_0	τ_1	θ_0	θ_1
Basal <a>	95	90	4000	80
Prismatic <a>	148	60	100	80
Pyramidal <c + a>	170	90	600	70
{10–12} twinning	100	40	600	50

Voce hardening model are obtained by fitting the true stress-strain curve in Fig. 15a. The hardening parameters used in this study are detailed in Table 6. For performing the VPSC simulation, the grain orientation list of the ES sample is used as input data. It is obtained through ATEX software by discretizing the initial EBSD texture of the ES sample (Fig. 3b) to 5000 orientations.

As shown in Fig. 15a, the strain-stress curve calculated by VPSC is well fitted with the experimental one. The relative activation of slip and twinning systems of the ES sample is presented in Fig. 15b. The results indicate that slip and twinning are both immediately activated after yielding. As tensile strain accumulates, the probabilities of twinning and prismatic slip activation gradually decrease, while basal slip activation increases continuously. The relative activity of $\langle c + a \rangle$ pyramidal slip firstly increases and then slowly decreases. At room temperature, non-basal slip is typically difficult to activate in Mg alloys during plastic deformation, which may be related to the activation of twinning in the early stages of tension. At the fracture strain, the texture of the ES sample was simulated and presented in Fig. 15c. The simulation results of texture evolution are well reproduced, and the rotation angle of the C1 texture is also equal to 21°. The simulation results match the experimental results in Fig. 14f, further validating the accuracy of the VPSC simulation results.

For the ES sample, the individual texture components of the multipolar texture can promote distinct activation of deformation mechanisms during tensile straining. The contribution of the individual texture components to the yield strength is also different. Therefore, the texture components of the ES samples need to be separated and individually analyzed. By considering the relationship between the c-axis of grains and the ED/ND in the ES sample, grains corresponding to the C1, C2, and P texture components are successfully separated from the EBSD data. These grain orientations are then discretized into 5000 orientation datasets for uniaxial tensile simulations. The discretized textures and VPSC-calculated relative activities of slip and twinning under tension are shown in Fig. 16a-c. For comparison, the dominant extrusion basal texture in the EX sample is similarly processed (Fig. 16d). The simulation results for single texture components reveal that the C1 texture promotes the activation of twinning and prismatic slip at the initial stages of tensile deformation in the ES sample. As tensile strain increases, the probability of twinning activation in C1-oriented grains decreases, while basal and pyramidal slip activation increases. During the tensile test, C1-oriented grains primarily undergo prismatic slip, with basal slip becoming dominant as strain accumulates. The C2 texture maintains a basal slip activation probability of approximately 0.55, with pyramidal slip activation around 0.4. For

Please cite this article as: D. Han, Z. Li, Z. Shi et al., Achieving strength-ductility-biodegradation synergy in a low-alloyed Mg-Sn-Li-Ca alloy via multi-polarization of texture and second phases, Journal of Magnesium and Alloys, https://doi.org/10.1016/j.jma.2026.102000

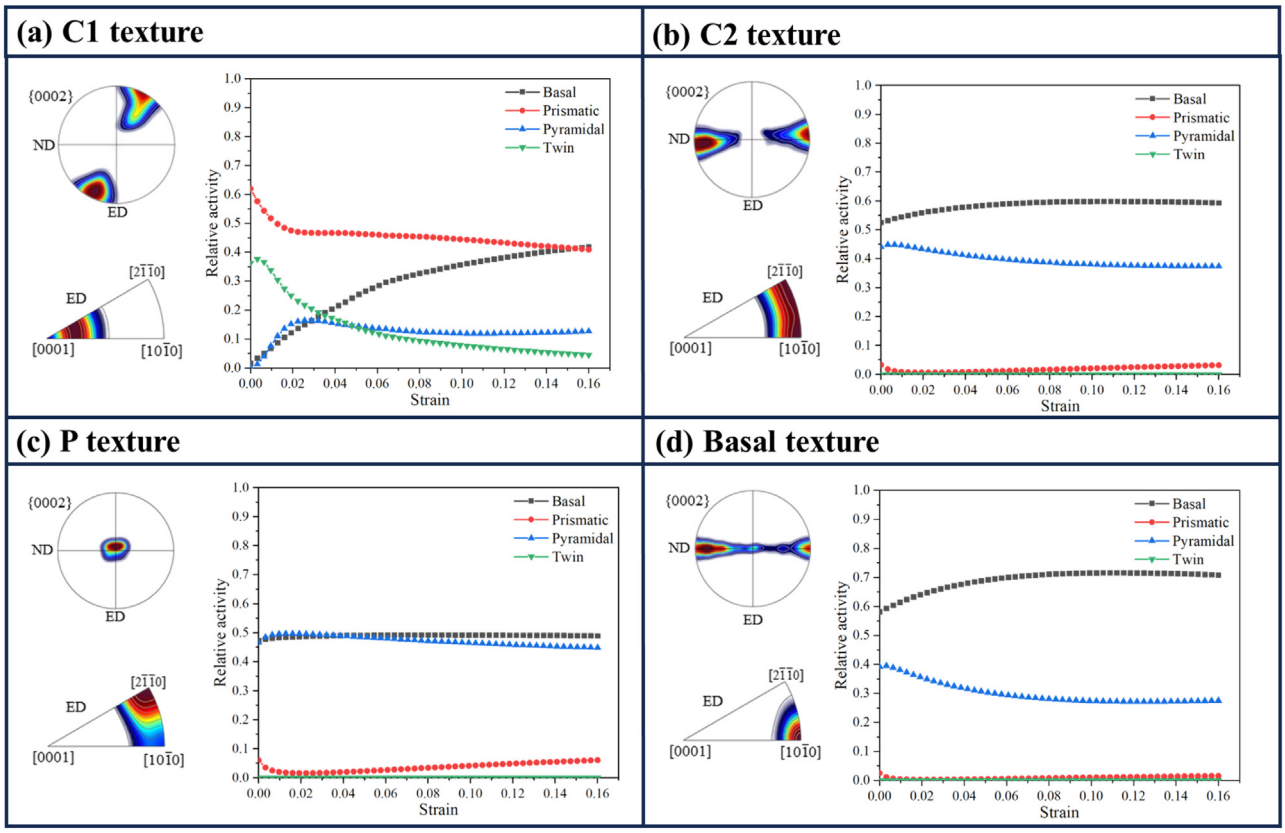

Fig. 16. VPSC simulation for the four individual texture components with relative activation of the different deformation mechanisms: (a) C1 texture; (b) C2 texture; (c) P texture and (d) [10–10]//ED fiber texture.

the corresponding grains of the P texture component, their specific orientation favors both pyramidal $\langle c + a \rangle$ slip and basal slip activation. In addition, as shown in Fig. 16d, the [10–10] fiber texture component in the EX sample has a similar effect on deformation mechanisms as the C2 texture, but with a higher probability of basal slip activation compared to pyramidal $\langle c + a \rangle$ slip. Prismatic slip and twinning are rarely activated in C2 and the conventional extrusion fiber. The calculated yield strengths for the C1, C2, P, and [10–10]//ED texture components are 183.9 MPa, 246.1 MPa, 247.7 MPa, and 248.2 MPa, respectively. It can be concluded that the C1 texture component benefits the ductility of the ES sample through twinning activation. The C2 and P texture components guaranteed the yield stress through the activation of basal and pyramidal slips.

Fig. 17 shows the evolution of the C1 texture during tensile deformation. When the applied von Mises equivalent strain reaches 0.03 in the VPSC simulation, the texture of the alloy remains almost unchanged. At this stage, the activation probabilities of basal slip, $\langle c + a \rangle$ slip, and twinning are equal, shown in Fig. 16a. This indicates that the texture evolution in the ES sample is not primarily driven by twinning or non-basal slip in the early stages during tension. When the simulated strain exceeds 0.08, the increased activation of basal slip takes the response for the rotation of C1 texture, eventually forming the RC1 texture.

4.3. Biodegradation mechanism

The immersion tests in α-MEM were conducted to explore the biodegradation mechanism optimization in the ES sample. Table 7 presents the biodegradation rates of ES and EX samples along with the ion concentrations in their extracts. The biodegradation rate of the ES sample is only ~68.2% of the ES sample, which aligns with the ratios of Mg^{2+}, Sn^{2+}, and Li^{+} ion concentrations between their extracts. The Volta potential difference (VPD) of the CaMgSn phase is approximately 150~170 mV higher than that of the Mg matrix [91], thereby hampering the release of Ca^{2+} ions. Furthermore, the released Ca^{2+} ions can form insoluble precipitates by reacting with phosphate salts in the α-MEM medium [92], leading to their negligible concentration variations.

Fig. 18a and b show the surface morphologies of the EX and the ES samples after removal of corrosion products. The EX sample shows more distinct pitting corrosion, whereas the ES sample exhibits a more uniform corrosion morphology. From the WLIM topographies, the dark blue areas indicate that the measured regions are >25 μm below the reference plane (0 μm), while the red areas represent regions that protrude approximately 10~25 μm above the reference plane. The corrosion surface of the EX sample exhibits extensive red areas and more than six dark blue points, indicating that its inferior corrosion resistance resulted in numerous deep pits

Please cite this article as: D. Han, Z. Li, Z. Shi et al., Achieving strength-ductility-biodegradation synergy in a low-alloyed Mg-Sn-Li-Ca alloy via multi-polarization of texture and second phases, Journal of Magnesium and Alloys, https://doi.org/10.1016/j.jma.2026.102000

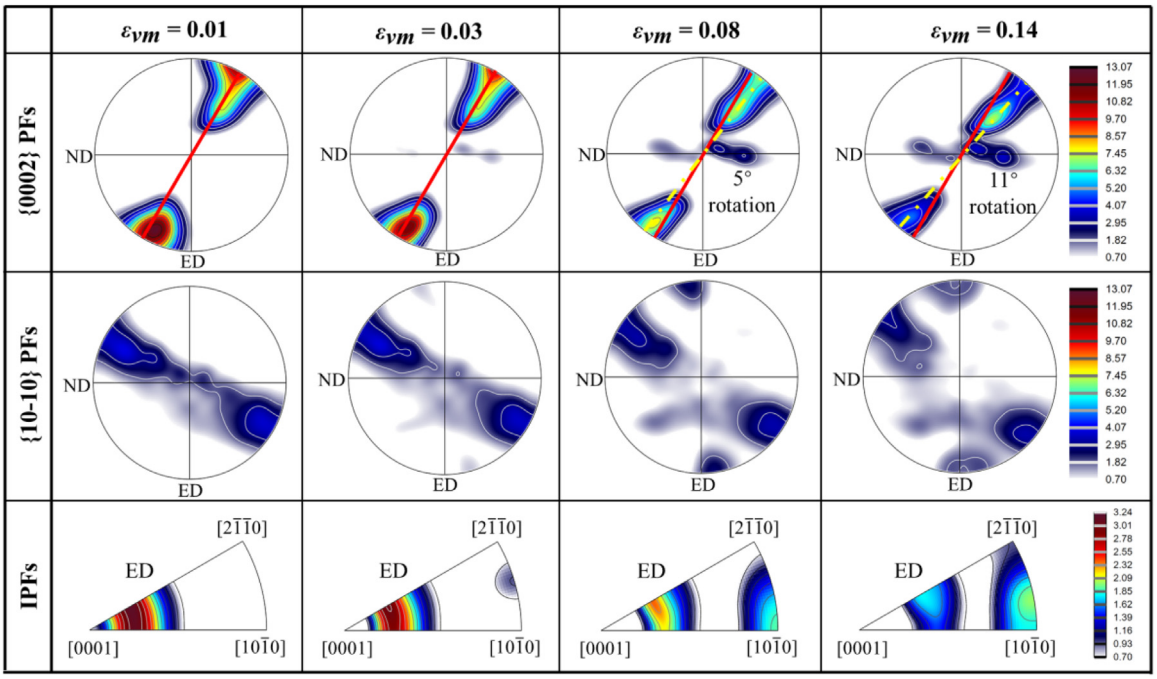

Fig. 17. C1 texture evolution with increasing tensile strain under VPSC simulation.

Table 7
Biodegradation rates and ion concentrations in 100% extracts.

Samples	biodegradation rates (mm/y)	Ion concentrations (mg/L)			
		Mg^{2+}	Sn^{2+}	Li^{+}	Ca^{2+}
ES	4.43 ± 0.40	176.62 ± 6.11	0.17 ± 0.02	1.12 ± 0.18	43.59 ± 3.57
EX	6.50 ± 2.38	243.02 ± 17.20	0.35 ± 0.04	1.70 ± 0.24	37.01 ± 3.35
α-MEM	——	14.38 ± 1.82	0.00 ± 0.00	0.00 ± 0.00	49.44 ± 1.54

and surface protrusions after immersion. In contrast, the ES sample shows neither pits deeper than 25 μm or pronounced surface protrusions. As shown in Fig. 18c and d, the maximum corrosion depth in the EX sample (43.31 μm) is 2.79 times that of the ES sample (15.53 μm). The EX specimen also exhibits a higher surface roughness (S_a = 3.47 μm) than that of the ES sample (S_a = 1.14 μm). This can be attributed to the non-linear distribution of second phases in the ES sample compared with the EX sample. As shown in the SEM images and the related biodegradation mechanism maps of Fig. 18e and f, the micro-galvanic is significantly reduced on the corrosion surface of the ES sample. Moreover, the ES sample shows a multipolar second-phase distribution. The resulting multidirectional and discontinuous streamlines of particles effectively impede the propagation of micro-galvanic corrosion along the ED. These results demonstrate that the multi-polarization of second-phase particles takes the main responsibility for the improvement of biodegradation resistance. In addition, the corrosion resistance of Mg alloys is also related to crystallographic planes. In the EX sample, the {10–10} extrusion fiber component is dominated, most {10–10} prismatic planes are oriented nearly parallel to the sample surface (i.e., the corrosion plane) under the immersion test. However, in grains with the C1 texture of the ES sample, the basal planes are rotated approximately 24° toward the corrosion plane, bringing the {1–217} planes nearly parallel to the surface. The corresponding crystal orientation schematics of the {10–10} extrusion fiber and the C1 component are presented in Fig. 18e and f, where the {0001} basal, {10–10} prismatic, and {1–217} planes are indicated. Previous studies [42,43] have reported that the basal plane exhibits superior corrosion resistance compared to the prismatic plane. It can be speculated that the {1–217} planes are also more corrosion-resistant.

4.4. Biocompatibility and osteogenic ability

Figs. 19a and 19b present cell viability (CV) values of MC3T3-E1 cells cultured for 1 day and 3 days in 25%∼100% concentration extracts, respectively. The CV values in all the extract concentrations exceed 75% and approach or surpass 100%, indicating that both the EX and the ES samples meet the non-toxicity criteria according to the ISO 10993-5 standard [68]. Fig. 19c shows live/dead staining images of MC3T3-E1 cells incubated in the extracts. The cells retain typical polygonal or spindle morphologies with prominent

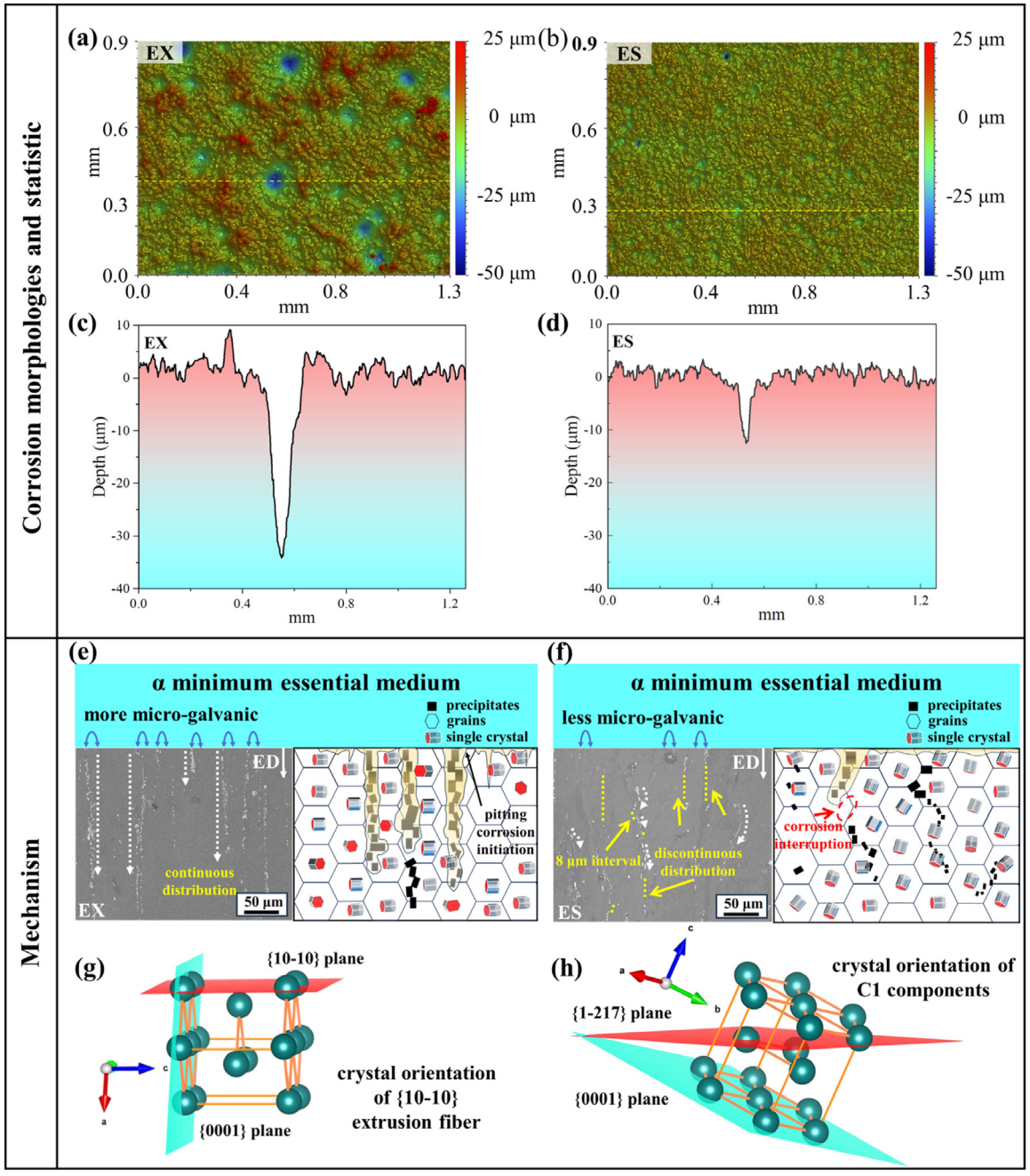

Fig. 18. (a, b) WLIM topographies and (c, d) depth profiles of immersed (a, c) EX and (b, d) ES samples after removal of corrosion products; the colors in WLIM maps show the height of the surface. Schematic of the biodegradation mechanism: (e) EX and (f) ES samples. (g, h) schematic of crystal orientations of {10–10} extrusion fiber and C1 texture components.

pseudopodia, reflecting maintained cell viability throughout the culture. There is no significant difference in cell densities between all the experimental groups and the negative control group. Dead cells are only observed in the positive control group. These results validate the superior biocompatibility of the TLX alloys (both EX and ES samples), which can also demonstrate their potential as orthopedic biomaterials.

ALP is an early marker of osteoblast differentiation. Fig. 20a presents ALP staining results of MC3T3-E1 cells cultured with 100% extracts for 4 and 7 days, and deeper purple staining indicates stronger ALP expression. After cultivation for 4 and 7 days, ALP expression levels in TLX (both EX and ES) groups are higher than that in the control group (α-MEM). Quantitative analysis of ALP activity (Fig. 19b) reveals that ALP activities in EX and ES show no significant difference and are consistently higher than the control group at both 4 and 7 days. These results indicate that 100% concentration extracts from the TLX alloys promote the osteogenic potential of MC3T3-E1 cells.

Please cite this article as: D. Han, Z. Li, Z. Shi et al., Achieving strength-ductility-biodegradation synergy in a low-alloyed Mg-Sn-Li-Ca alloy via multi-polarization of texture and second phases, Journal of Magnesium and Alloys, https://doi.org/10.1016/j.jma.2026.102000

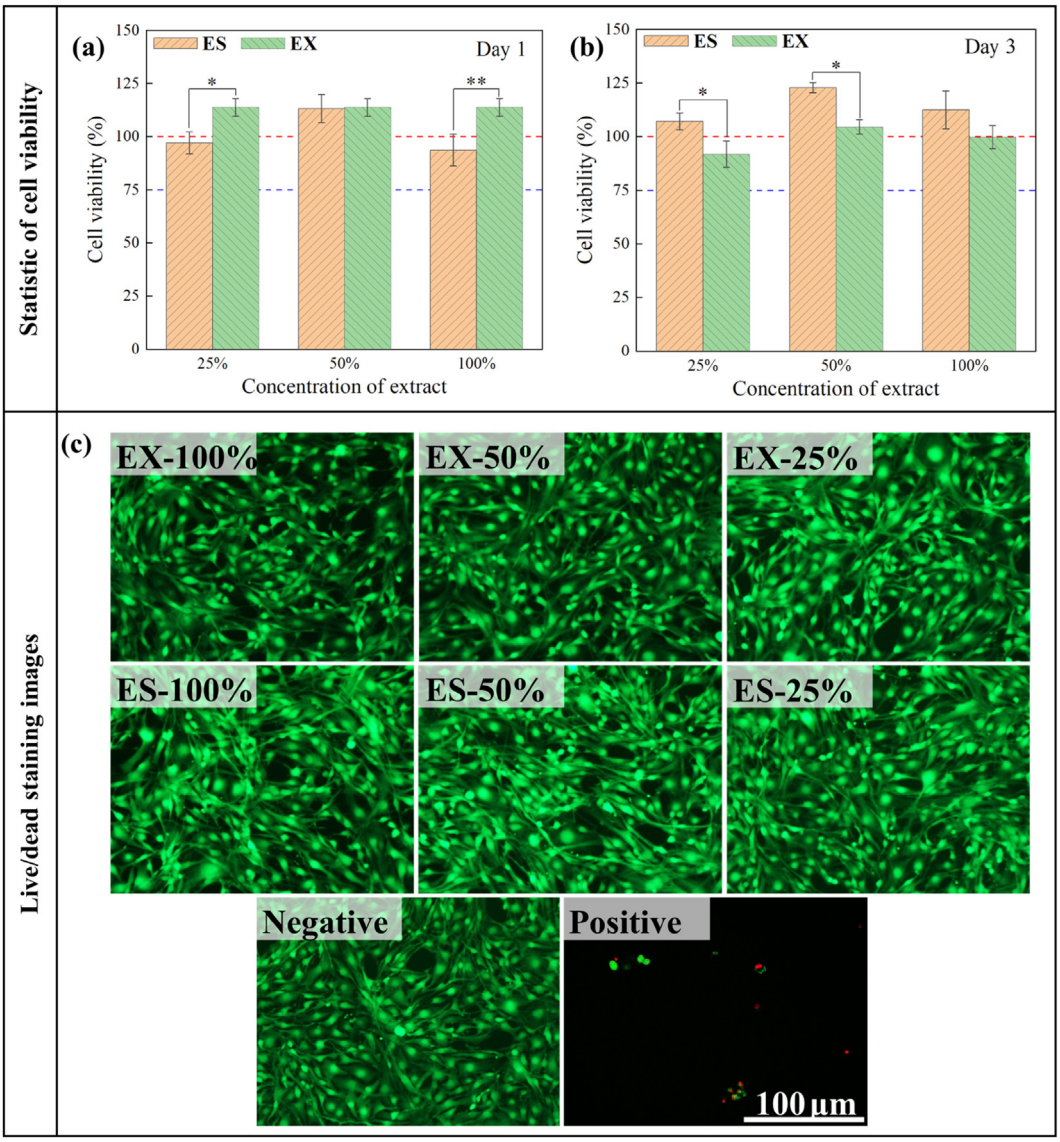

Fig. 19. Cell viability of MC3T3-E1 cells after incubation in 25%∼100% concentration extracts for (a) 1 day and (b) 3 days. (c) Live/dead staining images after 1-day incubation. (*denotes $p < 0.05$, **denotes $p < 0.01$).

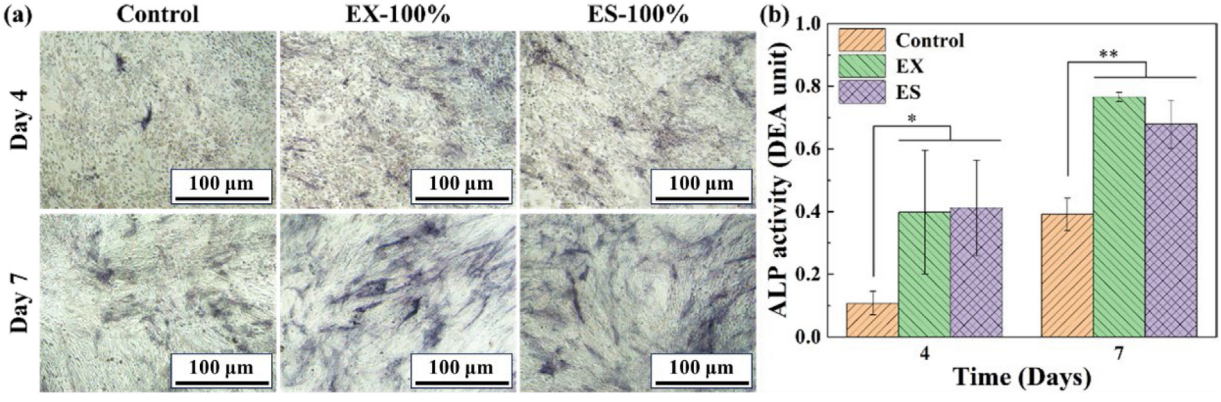

Fig. 20. MC3T3-E1 cells: (A) ALP staining results, (B) ALP activity.

Please cite this article as: D. Han, Z. Li, Z. Shi et al., Achieving strength-ductility-biodegradation synergy in a low-alloyed Mg-Sn-Li-Ca alloy via multi-polarization of texture and second phases, Journal of Magnesium and Alloys, https://doi.org/10.1016/j.jma.2026.102000

5. Conclusion

Adopting the strategy of coordinated optimization of the microstructure and texture, a low-alloyed Mg-Sn-Li-Ca alloy (TLX) with multipolar texture and second-phase distribution was successfully processed by the extrusion shearing process (ES). Compared with the conventional extrusion (EX) process under the same strain level, the ES samples show higher strength, ductility, better corrosion resistance, and balanced biocompatibility. The formation of texture multi-polarization, strengthening mechanisms, and improvement of biodegradation resistance were systematically revealed. The main findings are as follows:

(1) After being processed by EX or ES, the average grain size of the TLX alloy was refined to 11.1 μm and 4.9 μm, respectively. In both EX and ES samples, abundant Mg_2Sn and CaMgSn precipitates exist. Due to the extra ECAP process, the ES sample shows a multi-polarization of precipitate distribution with a slightly smaller particle size. In contrast to the conventional extrusion fiber texture of the EX sample, the ES sample shows a multipolar texture consisting of three shear texture components (C1, C2, and P) due to the activation of the pyramidal slip systems at the early stage of deformation.
(2) The tensile yield strength, ultimate tensile stress, and elongation of the ES sample are 231.8 MPa, 304.2 MPa, and 14.3%, which are improved by 10.4%, 16.3% and 24.3% compared to the EX sample, respectively. Based on the simulation results by using visco-plastic self-consistent modeling and the experimental microstructure evolution under tension, the contribution of individual texture components in the ES sample to strength and ductility is revealed. The C1 texture benefits the ductility by promoting the {10–12} twinning, while C2 and P texture components contribute to the high yield strength. The better strength-ductility synergy of the ES sample is achieved by the more uniform microstructure refinement and texture multi-polarization.
(3) Under the electrochemical corrosion and biological performance tests, the ES sample exhibits better corrosion resistance, lower biodegradation rate and the enhanced osteogenic capability. The multidirectional precipitation distribution impedes the micro-galvanic corrosion propagation along the particles in the ES sample, and the C1 texture component orients the basal planes more parallel to the sample surface.
(4) Through the coupled effects of grain refinement, texture and second-phase multi-polarization, the ES processed TLX alloy achieves a balanced improvement in strength, ductility, and biodegradation. This provides an effective microstructural design strategy for manufacturing high-performance biodegradable Mg alloy rods.

Acknowledgements

The authors are grateful for the financial support provided by the National Natural Science Foundation of China (grant numbers: 51901101 and 52271088). L.S. Toth was supported by the National Research, Development and Innovation Office, Hungary, under K143800 “New avenues of production of bulk and composite nanostructured metals; experiments, characterization, modeling”. Dongsheng HAN was supported by the Postgraduate Research & Practice Innovation Program of Jiangsu Province (grant number: SJCX25_0196).

Declaration of competing interest

The Authors declare that there are no conflicts or competing interests related to this work.

CRediT authorship contribution statement

Dongsheng Han: Writing – original draft, Visualization, Methodology, Investigation, Funding acquisition, Formal analysis, Data curation, Conceptualization. **Zilin Li:** Writing – original draft, Visualization, Methodology, Investigation, Data curation. **Zhangzhi Shi:** Writing – review & editing, Validation, Supervision, Project administration, Methodology, Funding acquisition, Data curation, Conceptualization. **Laszlo S Toth:** Writing – review & editing, Validation, Methodology, Data curation, Conceptualization. **Werner Skrotzki:** Writing – review & editing, Data curation. **Benoit Beausir:** Writing – review & editing, Validation, Software, Resources, Formal analysis, Data curation. **Zhonghua Du:** Writing – review & editing, Validation, Supervision, Resources. **Sen Yang:** Validation, Supervision, Resources. **Fengjian Shi:** Resources, Investigation. **Amélie Fillon:** Writing – review & editing, Resources. **Helene Birembaux:** Writing – review & editing. **Mohammed El Ganaoui:** Writing – review & editing, Validation, Supervision. **Cai Chen:** Writing – review & editing, Validation, Resources, Project administration, Methodology, Funding acquisition, Formal analysis, Data curation, Conceptualization. **Luning Wang:** Writing – review & editing, Validation, Resources.

References

[1] A. Malik, Y. Wang, C. Huanwu, F. Nazeer, M.A. Khan, J. Magnes. Alloy 9 (5) (2021) 1505–1520, doi:10.1016/j.jma.2020.07.011.
[2] S.J.B. Bin, K.S. Fong, B.W. Chua, M. Gupta, J. Magnes. Alloy 10 (4) (2022) 899–914, doi:10.1016/j.jma.2021.10.010.
[3] H. Wang, X.C. Luo, D.T. Zhang, C. Qiu, D.L. Chen, J. Mater. Sci. Technol. 199 (2024) 27–52, doi:10.1016/j.jmst.2024.01.089.
[4] J. Xie, T. Zhang, J. Jiang, W. Xue, W. Wang, J. Ni, X. Zhang, X. Liu, J. Magnes. Alloy 13 (7) (2025) 2978–3003, doi:10.1016/j.jma.2025.05.009.
[5] J. Dong, T. Lin, H. Shao, H. Wang, X. Wang, K. Song, Q. Li, J. Alloys Compd. 908 (2022) 164600, doi:10.1016/j.jallcom.2022.164600.
[6] Y. Luan, P. Mao, L. Tan, J. Sun, M. Gao, Z. Ma, Mater. Technol. 37 (8) (2021) 663–672, doi:10.1080/10667857.2020.1868747.
[7] W. Weng, A. Biesiekierski, Y. Li, M. Dargusch, C. Wen, Acta Biomater. 130 (2021) 80–97, doi:10.1016/j.actbio.2021.06.004.

Please cite this article as: D. Han, Z. Li, Z. Shi et al., Achieving strength-ductility-biodegradation synergy in a low-alloyed Mg-Sn-Li-Ca alloy via multi-polarization of texture and second phases, Journal of Magnesium and Alloys, https://doi.org/10.1016/j.jma.2026.102000

[8] M. Yang, C. Chen, D. Wang, Y. Shao, W. Zhou, C. Shuai, Y. Yang, X. Ning, J. Magnes. Alloy 12 (4) (2024) 1260–1282, doi:10.1016/j.jma.2024.03.014.
[9] R. Bao, J. Zhang, Y. He, Z. Li, S. Liu, H. Dong, Q. Yang, X. Zhang, X. Qiu, J. Magnes. Alloy (2025) available online, doi:10.1016/j.jma.2025.06.002.
[10] A.P. Loperena, S.B. Saidman, I.L. Lehr, Corrosion Communications 14 (2024), doi:10.1016/j.corcom.2023.08.004.
[11] X. Zhang, R. Zhou, C. Li, H. Yue, Q. Chen, J. Magnes. Alloy 13 (6) (2024) 2800–2812, doi:10.1016/j.jma.2024.08.008.
[12] Z. Yang, A. Ma, B. Xu, G. Wang, J. Jiang, J. Sun, J. Magnes. Alloy 13 (4) (2025) 1699–1720, doi:10.1016/j.jma.2024.06.032.
[13] F.J. Yao, B. Hu, J.X. Han, D.J. Li, Q.X. Zhang, D.L. Chen, X.Q. Zeng, J. Magnes. Alloy 13 (7) (2025) 2930–2958, doi:10.1016/j.jma.2025.05.010.
[14] M.G. Jiang, C. Xu, T. Nakata, H. Yan, R.S. Chen, S. Kamado, Mater. Sci. Eng. A 667 (2016) 233–239, doi:10.1016/j.msea.2016.04.093.
[15] S.J. Meng, H. Yu, S.D. Fan, Q.Z. Li, S.H. Park, J.S. Suh, Y.M. Kim, X.L. Nan, M.Z. Bian, F.X. Yin, W.M. Zhao, B.S. You, K.S. Shin, Acta Metall. Sin. (Engl. Lett.) 32 (2) (2019) 145–168, doi:10.1007/s40195-018-00871-2.
[16] H. Pan, G. Qin, Y. Huang, Y. Ren, X. Sha, X. Han, Z.Q. Liu, C. Li, X. Wu, H. Chen, C. He, L. Chai, Y. Wang, J.F. Nie, Acta Mater. 149 (2018) 350–363, doi:10.1016/j.actamat.2018.03.002.
[17] Z. Zhang, J. Xie, J. Zhang, X.S. Yang, R. Wu, J. Magnes. Alloy 12 (5) (2024) 1774–1791, doi:10.1016/j.jma.2024.03.016.
[18] Z. Cui, Y. Liu, Y. Zeng, M. Liu, X. Liu, S. Xu, X. Chen, Q. Wang, J. Magnes. Alloy 13 (1) (2025) 414–428, doi:10.1016/j.jma.2024.03.015.
[19] L. Wang, S. Hu, C. Xi, W. Zhou, T. Sakai, X. Yang, Q. Huo, J. Magnes. Alloy 13 (7) (2025) 3223–3236, doi:10.1016/j.jma.2024.12.002.
[20] J. Sun, W. Du, J. Fu, K. Liu, S. Li, Z. Wang, H. Liang, J. Magnes. Alloy 10 (10) (2022) 2649–2672, doi:10.1016/j.jma.2022.09.032.
[21] L. Tong, J. Jiang, G. Bi, Y. Li, T. Chen, X. Zhang, D. Fang, J. Magnes. Alloy 13 (6) (2025) 2825–2844, doi:10.1016/j.jma.2024.05.007.
[22] T. Zhou, Y. Li, F. Guo, Q. Li, Z. Jia, D. Liu, J. Magnes. Alloy 12 (11) (2024) 4622–4645, doi:10.1016/j.jma.2023.08.022.
[23] R. Fu, Y. Zeng, Y. Wan, X. Qian, S. Xu, D. Yin, J. Magnes. Alloy 13 (7) (2025) 3252–3270, doi:10.1016/j.jma.2025.02.030.
[24] C. Zhao, F. Pan, S. Zhao, H. Pan, K. Song, A. Tang, Mater. Des. 70 (2015) 60–67, doi:10.1016/j.matdes.2014.12.041.
[25] M. Shiri, H. Jafari, R. Singh, T. Nonferr. Metal. Soc. 32 (9) (2022) 2787–2813, doi:10.1016/s1003-6326(22)65984-3.
[26] R. Radha, D. Sreekanth, J. Magnes. Alloy 8 (2) (2020) 452–460, doi:10.1016/j.jma.2019.05.010.
[27] F.Z. Akbarzadeh, M. Sarraf, E.R. Ghomi, V.V. Kumar, M. Salehi, S. Ramakrishna, S. Bae, J. Magnes. Alloy 12 (7) (2024) 2569–2594, doi:10.1016/j.jma.2024.06.015.
[28] Y. Gong, J. He, J. Wen, W. Feng, X. Zheng, H. Li, Adv. Eng. Mater. 25 (12) (2023) 2201715, doi:10.1002/adem.202201715.
[29] T.A. Leil, N. Hort, W. Dietzel, C. Blawert, Y. Huang, K.U. Kainer, K.P. Rao, T. Nonferr. Metal. Soc. 19 (1) (2009) 40–44, doi:10.1016/s1003-6326(08)60225-3.
[30] C.Y. Zhao, F.S. Pan, H.C. Pan, T. Nonferr. Metal. Soc. 26 (6) (2016) 1574–1582, doi:10.1016/s1003-6326(16)64232-2.
[31] X.Y. Qian, Y. Zeng, B. Jiang, Q.R. Yang, Y.J. Wan, G.F. Quan, F.S. Pan, J. Alloys Compd. 820 (2020) 153122, doi:10.1016/j.jallcom.2019.153122.
[32] T. Zhou, B. Wang, Y. Li, S. Hu, X. Li, D. Liu, J. Mater. Sci. Technol. 199 (2024) 222–245, doi:10.1016/j.jmst.2024.01.095.
[33] S. Zhou, F. Wei, J. Wang, P. Jin, Mater. Res. Express 9 (9) (2022) 096517, doi:10.1088/2053-1591/ac9271.
[34] D. Bovand, H. Abdollah-Pour, O. Mirzaee, S. Bagherifard, J. Mater. Eng. Perform. 31 (8) (2022) 6835–6845, doi:10.1007/s11665-022-06727-2.
[35] J.H. Kim, J.W. Choi, Y.H. Kim, H.S. Yoo, K.D. Woo, S.H. Lee, H.T. Son, Int. J. Thermophys. 36 (10–11) (2015) 2666–2673, doi:10.1007/s10765-015-1912-5.
[36] Z. Pan, H. Pan, Y. Huang, Z. Zeng, Z.Z. Shi, C. Yang, Y. Ren, L.N. Wang, G. Qin, Prog. Nat. Sci.: Mater. Int. 33 (3) (2023) 355–363, doi:10.1016/j.pnsc.2023.08.021.
[37] Y. Jiang, Y.A. Chen, J. Gao, Mater. Des. 105 (2016) 34–40, doi:10.1016/j.matdes.2016.05.061.
[38] Y. Chai, L. Shan, B. Jiang, H. Yang, C. He, W. Hao, J. He, Q. Yang, M. Yuan, F. Pan, Prog. Nat. Sci.: Mater. Int. 31 (5) (2021) 722–730, doi:10.1016/j.pnsc.2021.08.007.
[39] X. Xiong, Y. Zeng, R. Fu, M. Liu, B. Jiang, J. Alloys Compd. 997 (2024) 174615, doi:10.1016/j.jallcom.2024.174615.
[40] C.Q. Liu, H.W. Chen, H. Liu, X.J. Zhao, J.F. Nie, Acta Mater. 144 (2018) 590–600, doi:10.1016/j.actamat.2017.10.023.
[41] Z. Chen, Y. Zhang, M. Ma, K. Zhang, Y. Li, G. Shi, J. Yuan, Z. Sun, G. Zhao, Mater. Chem. Phys. 300 (2023) 127500, doi:10.1016/j.matchemphys.2023.127500.
[42] Y. Xiong, Z. Yang, T. Zhu, Y. Jiang, Mater. Res. Express 7 (1) (2020) 015406, doi:10.1088/2053-1591/ab648c.
[43] G.L. Song, JOM 64 (6) (2012) 671–679, doi:10.1007/s11837-012-0341-1.
[44] D. Han, C. Chen, B. Beausir, Z. Du, S. Yang, M. Wang, R. Ren, F. Shi, Y. Zhou, W. Chen, W. Skrotzki, Z. Shi, L.S. Toth, J. Mater. Res. Technol. 36 (2025) 7881–7896, doi:10.1016/j.jmrt.2025.05.030.
[45] C.J. Yan, B. Guan, Y.C. Xin, L.Y. Zhao, G.J. Huang, R. Hong, X.B. Chen, P.K. Chu, Acta Metall. Sin. (Engl. Lett.) 36 (3) (2022) 439–455, doi:10.1007/s40195-022-01480-w.
[46] J. Wu, L. Jin, J. Dong, F. Wang, S. Dong, J. Mater. Sci. Technol. 42 (2020) 175–189, doi:10.1016/j.jmst.2019.10.010.
[47] J. Lin, X. Wang, W. Ren, X. Yang, Q. Wang, J. Mater. Sci. Technol. 32 (8) (2016) 783–789, doi:10.1016/j.jmst.2016.01.004.
[48] Y. Yao, C. Liu, Y. Wan, S. Yu, Y. Gao, S. Jiang, Mater. Charact. 161 (2020) 110120, doi:10.1016/j.matchar.2020.110120.
[49] J. Xu, Y. Peng, B. Guan, Y. Xin, A. Chapuis, G. Huang, Q. Liu, Mater. Sci. Eng. A 844 (2022) 143202, doi:10.1016/j.msea.2022.143202.
[50] D. Han, C. Chen, M. Wang, N. Siredey-Schwaller, Z. Du, S. Yang, F. Shi, B. Beausir, A. Tongne, L.S. Toth, Mater. Charact. 225 (2025) 115180, doi:10.1016/j.matchar.2025.115180.
[51] N. Lv, L. Zhao, H. Yan, B. Liu, Y. Mao, Z. Shan, R. Chen, J. Alloys Compd. 966 (2023) 171590, doi:10.1016/j.jallcom.2023.171590.
[52] Z. Yan, Z. Zhang, X. Li, J. Xu, Q. Wang, G. Zhang, J. Zheng, H. Fan, K. Xu, J. Zhu, Y. Xue, J. Alloys Compd. 822 (2020) 153698, doi:10.1016/j.jallcom.2020.153698.
[53] K. Edalati, A. Bachmaier, V.A. Beloshenko, Y. Beygelzimer, V.D. Blank, W.J. Botta, K. Bryła, J. Čížek, S. Divinski, N.A. Enikeev, Y. Estrin, G. Faraji, R.B. Figueiredo, M. Fuji, T. Furuta, T. Grosdidier, J. Gubicza, A. Hohenwarter, Z. Horita, J. Huot, Y. Ikoma, M. Janeček, M. Kawasaki, P. Král, S. Kuramoto, T.G. Langdon, D.R. Leiva, V.I. Levitas, A. Mazilkin, M. Mito, H. Miyamoto, T. Nishizaki, R. Pippan, V.V. Popov, E.N. Popova, G. Purcek, O. Renk, Á. Révész, X. Sauvage, V. Sklenicka, W. Skrotzki, B.B. Straumal, S. Suwas, L.S. Toth, N. Tsuji, R.Z. Valiev, G. Wilde, M.J. Zehetbauer, X. Zhu, Mater. Res. Lett. 10 (4) (2022) 163–256, doi:10.1080/21663831.2022.2029779.
[54] Y. Liu, D. Lu, G. Wu, Z. Zhang, H. Huang, L. Li, Y. Feng, J. Yu, J. Alloys Compd. 985 (2024) 174099, doi:10.1016/j.jallcom.2024.174099.
[55] M. Zemková, P. Minárik, J. Dittrich, J. Bohlen, R. Král, J. Magnes. Alloy 11 (2) (2023) 509–521, doi:10.1016/j.jma.2023.01.012.
[56] M. Hashemi, R. Alizadeh, T.G. Langdon, J. Magnes. Alloy 11 (7) (2023) 2260–2284, doi:10.1016/j.jma.2023.07.009.
[57] W. Cheng, L. Tian, H. Wang, L. Bian, H. Yu, Mater. Sci. Eng. A 687 (2017) 148–154, doi:10.1016/j.msea.2017.01.054.
[58] T. Zhou, B. Wang, M. Zhang, Y. Li, S. Hu, X. Li, D. Liu, Mater. Sci. Eng. A 899 (2024) 146469, doi:10.1016/j.msea.2024.146469.
[59] S. Prithivirajan, S. Narendranath, V. Desai, J. Magnes. Alloy 8 (4) (2020) 1128–1143, doi:10.1016/j.jma.2020.08.015.
[60] Y. Cubides, D. Zhao, L. Nash, D. Yadav, K. Xie, I. Karaman, H. Castaneda, J. Magnes. Alloy 8 (4) (2020) 1016–1037, doi:10.1016/j.jma.2020.09.005.

Please cite this article as: D. Han, Z. Li, Z. Shi et al., Achieving strength-ductility-biodegradation synergy in a low-alloyed Mg-Sn-Li-Ca alloy via multi-polarization of texture and second phases, Journal of Magnesium and Alloys, https://doi.org/10.1016/j.jma.2026.102000

[61] Y. Shen, J. Chen, G. Wang, D. Cao, L. Tan, R.D.K. Misra, K. Yang, Mater. Technol. 37 (2) (2020) 135–142, doi:10.1080/10667857.2020.1816384.
[62] Z. Sun, Y. Li, M. Ma, X. Li, G. Shi, J. Yuan, D. Chen, K. Zhang, Mater. Lett. 357 (2024) 135775, doi:10.1016/j.matlet.2023.135775.
[63] N. Martynenko, E. Lukyanova, V. Serebryany, D. Prosvirnin, V. Terentiev, G. Raab, S. Dobatkin, Y. Estrin, Mater. Lett. 238 (2019) 218–221, doi:10.1016/j.matlet.2018.12.024.
[64] M.M. Hoseini-Athar, R. Mahmudi, R. Prasath Babu, P. Hedström, Scr. Mater. 186 (2020) 253–258, doi:10.1016/j.scriptamat.2020.05.042.
[65] C. Chen, D. Han, M. Wang, S. Xu, T. Cai, S. Yang, F. Shi, B. Beausir, L.S. Toth, J. Alloys Compd. 931 (2023) 167498, doi:10.1016/j.jallcom.2022.167498.
[66] Z. Shi, A. Atrens, Corros. Sci. 53 (1) (2011) 226–246, doi:10.1016/j.corsci.2010.09.016.
[67] Z.L. Li, Z.Z. Shi, W.L. Cai, J.Y. Wang, X.J. Ji, F.Z. Dai, X.F. Gu, L.N. Wang, J. Alloys Compd. 1026 (2025) 180460, doi:10.1016/j.jallcom.2025.180460.
[68] X.J. Ji, K. Yang, S.L. Yao, H. Zhang, K.W. Gao, Z.Z. Shi, D. Xu, L.N. Wang, J. Mater. Sci. Technol. 237 (2025) 20–37, doi:10.1016/j.jmst.2024.12.053.
[69] B. Beausir, J.J. Fundenberger, Analysis Tools For Electron and X-ray diffraction, ATEX-software, Université de Lorraine - Metz, 2017 www.atex-software.eu.
[70] J.K. Mason, C.A. Schuh, Acta Mater. 57 (14) (2009) 4186–4197, doi:10.1016/j.actamat.2009.05.016.
[71] J. Wang, J. Han, I.H. Jung, D. Bairos, P. Chartrand, Calphad 47 (2014) 100–113, doi:10.1016/j.calphad.2014.07.001.
[72] G. Zhou, Y. Yang, H. Zhang, F. Hu, X. Zhang, C. Wen, W. Xie, B. Jiang, X. Peng, F. Pan, J. Mater. Sci. Technol. 103 (2022) 186–196, doi:10.1016/j.jmst.2021.07.009.
[73] B. Beausir, L.S. Tóth, K.W. Neale, Acta Mater. 55 (8) (2007) 2695–2705, doi:10.1016/j.actamat.2006.12.021.
[74] B. Beausir, S. Suwas, L.S. Tóth, K.W. Neale, J.J. Fundenberger, Acta Mater. 56 (2) (2008) 200–214, doi:10.1016/j.actamat.2007.09.032.
[75] J. Wang, M.R.G. Ferdowsi, S.R. Kada, S. Babaniaris, B. Hutchinson, P.A. Lynch, M.R. Barnett, Scr. Mater. 210 (2022) 114422, doi:10.1016/j.scriptamat.2021.114422.
[76] C. Zhao, X. Chen, F. Pan, S. Gao, D. Zhao, X. Liu, Mater. Sci. Eng. A 713 (2018) 244–252, doi:10.1016/j.msea.2017.12.074.
[77] W.N. Tang, S.S. Park, B.S. You, Mater. Des. 32 (6) (2011) 3537–3543, doi:10.1016/j.matdes.2011.02.012.
[78] Y. Chai, B. Jiang, J. Song, Q. Wang, H. Gao, B. Liu, G. Huang, D. Zhang, F. Pan, J. Alloys Compd. 782 (2019) 1076–1086, doi:10.1016/j.jallcom.2018.12.109.
[79] Y. Luo, Y. Chen, L. Ran, X. Pang, F. Pan, Mater. Sci. Eng. A 815 (2021) 141307, doi:10.1016/j.msea.2021.141307.
[80] B. Kim, S.-M. Baek, H.Y. Jeong, J.G. Lee, S.S. Park, J. Alloys Compd. 660 (2016) 304–309, doi:10.1016/j.jallcom.2015.11.133.
[81] S. Jayalakshmi, S. Sankaranarayanan, S.P.X. Koh, M. Gupta, J. Alloys Compd. 565 (2013) 56–65, doi:10.1016/j.jallcom.2013.02.186.
[82] Y. Chen, L. Jin, Y. Song, H. Liu, R. Ye, Mater. Sci. Eng. A 612 (2014) 96–101, doi:10.1016/j.msea.2014.06.022.
[83] J. Wu, L. Wu, W. Yao, Y. Chen, Y. Zhou, M. Wu, Y. Yuan, Z. Xie, J. Wang, F. Pan, Corros. Sci. 224 (2023) 111511, doi:10.1016/j.corsci.2023.111511.
[84] Z.J. Jiao, C.Y. Li, Y.K. Du, L.Y. Cui, X.B. Chen, Y.M. Xi, R.C. Zeng, Surf. Coat. Tech. 472 (2023) 129922, doi:10.1016/j.surfcoat.2023.129922.
[85] T. Sakai, A. Belyakov, R. Kaibyshev, H. Miura, J.J. Jonas, Prog. Mater. Sci. 60 (2014) 130–207, doi:10.1016/j.pmatsci.2013.09.002.
[86] X. Wang, M. Gao, L. Miao, L. Tan, K. Yang, Mater. Today Commun. 38 (2024) 107928, doi:10.1016/j.mtcomm.2023.107928.
[87] T. Li, J. Zheng, M. Gupta, L. Xia, L. He, S. Liu, D. Xia, J. Luo, B. Jiang, Mater. Sci. Eng. A 888 (2023) 107928, doi:10.1016/j.msea.2023.107928.
[88] W. Yuan, S.K. Panigrahi, J.Q. Su, R.S. Mishra, Scr. Mater. 65 (11) (2011) 994–997, doi:10.1016/j.scriptamat.2011.08.028.
[89] Y. Lyu, I.P. Jones, Y.L. Chiu, Philos. Mag. 102 (16) (2022) 1580–1601, doi:10.1080/14786435.2022.2079749.
[90] Z. Liu, R. Xin, X. Huang, J. Mater. Sci. 59 (2024) 10058–10077, doi:10.1007/s10853-024-09572-x.
[91] Y.J. Li, M.X. Li, B.Y. Wang, M.W. Ren, C. Wang, M. Zha, Y. Gao, H.Y. Wang, Corros. Sci. 235 (2024) 112180, doi:10.1016/j.corsci.2024.112180.
[92] A.S. Gnedenkov, S.L. Sinebryukhov, V.S. Filonina, V.S. Egorkin, A.Y. Ustinov, V.I. Sergienko, S.V. Gnedenkov, J. Magnes. Alloy 10 (5) (2022) 1326–1350, doi:10.1016/j.jma.2021.11.027.

Please cite this article as: D. Han, Z. Li, Z. Shi et al., Achieving strength-ductility-biodegradation synergy in a low-alloyed Mg-Sn-Li-Ca alloy via multi-polarization of texture and second phases, Journal of Magnesium and Alloys, https://doi.org/10.1016/j.jma.2026.102000